

12 MARCH 2025

Science Translational Medicine

INTERSTITIAL LUNG DISEASE

A human histidyl-tRNA synthetase splice variant therapeutic targets NRP2 to resolve lung inflammation and fibrosis

Leslie A. Nangle^{1*}, Zhiwen Xu¹, David Siefker¹, Christoph Burkart¹, Yeeting E. Chong¹, Liting Zhai^{2,3†}, Yanyan Geng^{2,3‡}, Clara Polizzi¹, Lauren Guy¹, Lisa Eide^{1§}, Yao Tong^{2,3¶}, Sofia Klopp-Savino¹, Michaela Ferrer^{1#}, Kaitlyn Rauch¹, Annie Wang¹, Kristina Hamel¹, Steve Crampton^{1**}, Suzanne Paz^{1††}, Kyle P. Chiang^{1‡‡}, Minh-Ha Do^{1§§}, Luke Burman¹, Darin Lee¹, Mingjie Zhang², Kathleen Ogilvie^{1¶¶}, David King^{1###}, Ryan A. Adams¹, Paul Schimmel^{4*}

Copyright © 2025 The Authors, some rights reserved; exclusive licensee American Association for the Advancement of Science. No claim to original U.S. Government Works

Interstitial lung disease (ILD) consists of a group of immune-mediated disorders that can cause inflammation and progressive fibrosis of the lungs, representing an area of unmet medical need given the lack of disease-modifying therapies and toxicities associated with current treatment options. Tissue-specific splice variants (SVs) of human aminoacyl-tRNA synthetases (aaRSs) are catalytic nulls thought to confer regulatory functions. One example from human histidyl-tRNA synthetase (HARS), termed HARS^{WHEP} because the splicing event resulted in a protein encompassing the WHEP-TRS domain of HARS (a structurally conserved domain found in multiple aaRSs), is enriched in human lung and up-regulated by inflammatory cytokines in lung and immune cells. Structural analysis of HARS^{WHEP} confirmed a well-organized helix-turn-helix motif. This motif bound specifically and selectively to neuropilin-2 (NRP2), a receptor expressed by myeloid cells in active sites of inflammation, to inhibit expression of proinflammatory receptors and cytokines and to down-regulate inflammatory pathways in primary human macrophages. In animal models of lung injury and ILD, including bleomycin treatment, silicosis, sarcoidosis, chronic hypersensitivity pneumonitis, systemic sclerosis, and rheumatoid arthritis-ILD, HARS^{WHEP} reduced lung inflammation, immune cell infiltration, and fibrosis. In patients with sarcoidosis, efzofitmod treatment resulted in down-regulation of gene expression for inflammatory pathways in peripheral immune cells and stabilization of inflammatory biomarkers in serum after steroid tapering. We demonstrate the immunomodulatory activity of HARS^{WHEP} and present preclinical data supporting ongoing clinical development of the biologic efzofitmod based on HARS^{WHEP} in ILD.

INTRODUCTION

Despite diverse disease triggers, interstitial lung diseases (ILDs) are a group of immune-mediated disorders that are all associated with progressive fibrosis, or scarring, of the lung (1, 2) and vary in the relative amounts of immune involvement in the chronic conditions. Chronic inflammation and tissue scarring stiffen the lung, impairing breathing and leading to progressive and irreversible damage. More than 500,000 patients have ILDs in the United States, and upward of 3 million are estimated globally (3). Within the more than 200

different types of ILDs, four account for roughly 80% of all patients (4). Ranked from most to least inflammatory, these four types of disease are pulmonary sarcoidosis; chronic hypersensitivity pneumonitis (CHP); connective tissue disease-associated ILD, including systemic sclerosis (SSc)-associated ILD; and idiopathic pulmonary fibrosis. Current treatment options are limited and generally focused on palliative control of inflammation, with targeted antifibrotic therapies approved for use in select patients, highlighting an unmet medical need for ILDs.

Recent years have seen growing awareness of the roles of aminoacyl-tRNA synthetases (aaRSs) in health and disease (5–8). Given that these ancient proteins establish the rules of the genetic code through their aminoacylation reactions, it was unexpected to discover a large array of previously unknown orthogonal functions linked to these enzymes (9). These functions include roles in signaling pathways ranging from angiogenesis, transcription control, oncogenesis, neurology, inflammation, RNA splicing, and more (10–17). Associated with these functions is the acquisition in eukaryotic evolution of new noncatalytic domains in the aaRSs. These domains are progressively added in eukaryotes as the tree of life is ascended and, once added, remain as part of the aaRSs (18, 19). These domains are either idiosyncratic to the specific aaRS or are shared as structural homologs by a limited subset of the enzymes. As an example, in a vertebrate model, a specific appended domain that is unique to seryl-tRNA synthetase was shown to be essential for normal development of a closed vascular system (20).

There are more than 100 aaRS genetic mutations in the human population that are causally linked to disease (21–24), which include homozygous recessive, compound heterozygous and dominant, and

¹aTyr Pharma, San Diego, CA 92121, USA. ²IAS HKUST–Scripps R&D Laboratory, Institute for Advanced Study, Hong Kong University of Science and Technology, Clear Water Bay, Kowloon, Hong Kong, China. ³Pangu Biopharma, Hong Kong, China. ⁴Department of Molecular Medicine, Scripps Research Institute, La Jolla, CA 92037, USA.

*Corresponding author. Email: lnangle@atyrpharma.com (L.A.N.); schimmel@scripps.edu (P.S.)

†Present address: Chinese University of Hong Kong, Ma Liu Shui, Hong Kong, China.

‡Present address: Clinical Research Institute, First Affiliated Hospital of Xiamen University, Fujian Key Laboratory of Brain Tumors Diagnosis and Precision Treatment, Xiamen Key Laboratory of Brain Center, First Affiliated Hospital of Xiamen University, School of Medicine, Xiamen University, Xiamen, Fujian, China.

§Present address: Contineum Therapeutics, San Diego, CA 92121, USA.

¶Present address: Department of Molecular Medicine, Scripps Research Institute, La Jolla, CA 92037, USA.

#Present address: Korsia Therapeutics, San Diego, CA 92130, USA.

**Present address: Janssen Pharmaceutical Companies of Johnson & Johnson, San Diego, CA 92123, USA.

††Present address: Nerio Therapeutics, La Jolla, CA 92037, USA.

‡‡Present address: Flagship Pioneering, Cambridge, MA 02142, USA.

§§Present address: Rampart Bioscience, Monrovia, CA 91016, USA.

¶¶Present address: Ventyx Biosciences, San Diego, CA 92130, USA.

###Present address: Lassen Therapeutics, San Diego, CA 92121, USA.

gain-of-function mutations. These mutations can appear well outside the active site region and do not always cause a disruption of the catalytic function (24). Possibly related to these disease-causing mutations are the more than 200 splice variants (SVs) that have been reported for human aARs (25). These variants are expressed in a developmental stage-specific and tissue-specific fashion and can be found extracellularly released by unconventional secretion mechanisms. Most variants are catalytic nulls, ablating or partially resecting the active site but retaining the newly appended or inserted domain. In a screen of an array of cell signaling assays, in which purified protein versions representing translated SVs were applied extracellularly, many of the SVs induced cell type-specific activities likely mediated through interactions with cell surface receptors (25). These activities suggested possible applications for at least some SVs in a therapeutic setting. Thus, we focused on more thoroughly characterizing and developing one promising SV of human histidyl-tRNA synthetase (HARS), which is associated with a well-studied pathological condition, as a proof of principle for this class of molecules that had never been evaluated in human clinical trials.

The N-terminal domain of HARS is targeted by autoantibodies in a rare autoimmune disorder known as anti-Jo-1 syndrome (26, 27). This syndrome is characterized by extensive activation and migration of immune cells into the lung and muscle and is classically associated with the triad of ILD, myositis, and arthritis (28). Although HARS has been shown to circulate in healthy individuals, it is largely undetectable in the sera of patients positive for anti-Jo-1 antibodies (14). The apparent sequestration of extracellular HARS is hypothesized to play a causal role through disruption of its homeostatic immune-regulatory effects. The autoantibody reactive N-terminal WHEP domain of HARS (a motif present in several human aARs that is structurally but not sequence conserved in this family of enzymes) was appended to the core catalytic domain (CD) through its appearance in the genome with the evolution of nematodes (18). The helix-turn-helix (HTH) motif (amino acids 1 to 48) of this domain was originally reported as a proteolytic fragment liberated by granzyme B cleavage from HARS in the lung (29). Subsequent data showed that the HARS WHEP domain also appears as an SV (HARS^{WHEP}) that is enriched in human lung tissue and secreted from immune cells (30). Given these findings, we raised the question of whether this HARS SV conveys a homeostatic immunomodulatory function and could be used in a therapeutic setting for inflammatory disorders. We chose to focus on the forms of ILD associated with chronic inflammation to probe the therapeutic potential of this aAR SV. Hence, a therapeutic form based on HARS^{WHEP} engineered to confer extended serum exposure (HARS^{WHEP}-Fc/efzofitimid) was developed and evaluated in preclinical studies and eventually in a phase 1b/2a clinical study in patients with pulmonary sarcoidosis, a form of inflammatory ILD, demonstrating a promising safety profile and dose-dependent improvement in efficacy parameters for lung function and quality of life (31–33).

RESULTS

Inflammatory cytokines induce HARS^{WHEP} up-regulation and secretion in lung cells

Previous work has shown that the HARS^{WHEP} SV is enriched in human lung tissue (30). We therefore studied cytokine regulation of HARS^{WHEP} expression and secretion in the human lung alveolar type II pulmonary epithelial cell line A549, given that this type of cell contributes to the pathogenesis of ILD (34, 35). A panel of six proinflammatory,

anti-inflammatory, or fibrotic cytokines was screened in singlets and all possible combinations for the stimulation of A549 (table S1). Among the one- or two-cytokine treatments, HARS proteins containing the N-terminal WHEP domain (N-HARS such as HARS^{WHEP}) were actively secreted after stimulation with the inflammatory cytokines tumor necrosis factor- α (TNF- α) and interferon- γ (IFN- γ ; fig. S1A). These two cytokines are key contributors to the initiation of lung inflammation and fibrosis. Secretion was time dependent along with the cell morphology change from an epithelial-like appearance to a mesenchymal-like spindle cell shape (Fig. 1A and fig. S1A), indicating an epithelial-mesenchymal transition (EMT) that has been associated with pathogenesis of fibrotic disorders (36, 37). The release of N-HARS was also observed with most combinations of three or more cytokines in the screen (table S1). In a time-course study, TNF- α and IFN- γ also selectively induced the up-regulation of HARS^{WHEP} but not of full-length (FL) HARS mRNA ($P < 0.0001$; Fig. 1A). The HARS^{WHEP} transcript increased after inflammatory cytokine stimulation and, as expected, peak expression preceded that of the secreted protein. These results established a notable cytokine dependence for expression of HARS^{WHEP} mRNA and for subsequent secretion of the translated protein, whose production was decoupled from HARS_{FL} mRNA expression.

HARS^{WHEP} adapted to a therapeutic modality retains structural conformation of natural SV

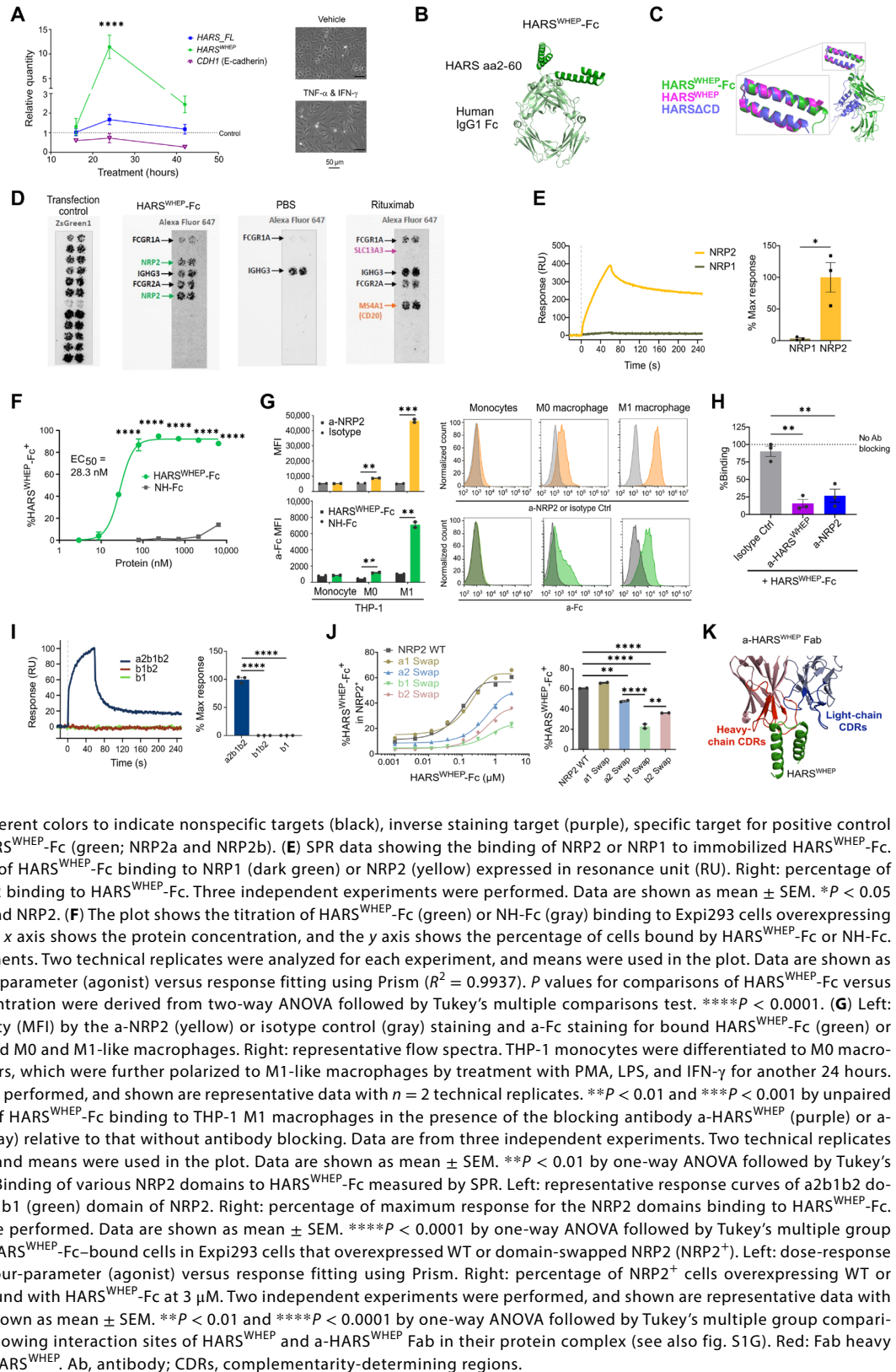
On the basis of our data, we expected that the secreted HARS^{WHEP} protein would be released locally at inflammatory sites and exhibit a relatively short serum half-life given its small size. To generate a more therapeutically relevant molecule and establish the potential for in vivo testing, we fused the HARS WHEP domain amino acids 2 to 60 to the Fc region of human immunoglobulin G1 (IgG1) (HARS^{WHEP}-Fc). The protein was expressed in *Escherichia coli* cells in insoluble inclusion bodies, subject to refolding; purified; and confirmed to form a dimer in solution (fig. S1B).

A structure determined by nuclear magnetic resonance (NMR) revealed an HTH motif for the HARS WHEP domain [Protein Data Bank (PDB): 1X59]. Earlier work also investigated the three-dimensional (3D) NMR structure of another human HARS SV, which linked the WHEP domain to the C-terminal anticodon binding domain (38). This natural SV with the protein designated as HARS Δ CD skips the entire CD and purifies as a monomer. Unlike monomeric HARS WHEP alone or HARS Δ CD, HARS^{WHEP}-Fc is a dimer because of the inclusion of an IgG1-Fc domain to provide half-life extension in serum. This distinction provided some motivation to investigate further the conformation of the WHEP domain in HARS^{WHEP}-Fc, especially to see if it was altered by dimer formation. We were able to crystallize HARS^{WHEP}-Fc and to obtain a 2.8-Å structure (Fig. 1B and table S2). This structure confirmed that dimerization occurs through the Fc chains and that the WHEP domain itself is free of contacts with those chains. When the NMR structures of the WHEP domain alone (PDB: 1X59) and the WHEP in HARS Δ CD (PDB: 2LW7) were overlaid with that of the crystal structure of HARS^{WHEP}-Fc reported here, the superpositions had root mean square deviations of 0.779 and 1.324 Å, respectively (Fig. 1C). Thus, the WHEP domain of HARS^{WHEP}-Fc is relatively unperturbed by the presence of the Fc portion.

NRP2 is the specific target receptor for HARS^{WHEP} on immune cells

To identify a possible receptor for HARS^{WHEP}, we took advantage of the library of more than 4500 human membrane proteins assembled

Fig. 1. Newly evolved SV of HARS was expressed in inflammation and selectively bound NRP2. (A) Relative quantity of mRNA expression in cytokine-treated A549 cells to that in vehicle-treated control for *HARS_FL*, *HARS^{WHEP}*, and *CDH1*. Lung A549 cells were treated with the inflammatory cytokines TNF- α and IFN- γ . Left: plot of a time-course study with cells treated for 16, 24, and 42 hours. *n* = 3 biological replicates. Data are shown as mean \pm SEM. *****P* < 0.0001 for *HARS^{WHEP}* versus *HARS_FL* by two-way ANOVA followed with Tukey's multiple comparisons test. Right: representative images of the A549 morphology at 42 hours posttreatment with vehicle or cytokines. Scale bars, 50 μ m.



Downloaded from https://www.science.org at Scripps Research Institute on March 12, 2025

by Retrogenix Biotechnology Company (now part of Charles River Laboratories). In screening through this library by staining and immunofluorescence (IF) detection of bound HARS^{WHEP}-Fc on human embryonic kidney (HEK) 293 cells overexpressing each of the membrane proteins, neuropilin-2a (NRP2a) and NRP2b isoforms of the NRP2 receptor were identified as the sole validated binding targets for HARS^{WHEP}-Fc (Fig. 1D and table S3). NRP2 is a pleiotropic receptor with functional roles in the cardiovascular, nervous, and immune systems (39). In the screen, no binding was detected for the related and structurally similar receptor NRP1 (45% sequence identity to NRP2). The specificity of HARS^{WHEP}-Fc for binding NRP2 but not NRP1 was confirmed by surface plasmon resonance (SPR) measurements ($P = 0.0146$; Fig. 1E). In further work, we found that HARS^{WHEP}-Fc bound with a median effective concentration (EC₅₀) around 30 nM to NRP2 overexpressed on HEK Expi293 cells (Fig. 1F). A control protein NH-Fc (IgG1-Fc fused with only amino acids 2 to 11 of HARS^{WHEP} and missing amino acids 12 to 60) showed little binding to these cells.

Next, we took advantage of the finding that cell surface NRP2 expression was up-regulated during THP-1 differentiation from monocytes to M0 macrophages by the treatment of phorbol 12-myristate 13-acetate (PMA) ($P < 0.01$). The up-regulation was especially prominent on M1-like macrophages further polarized with lipopolysaccharide (LPS) and IFN- γ (Fig. 1G). We found that HARS^{WHEP}-Fc bound to THP-1 M0 and M1-like macrophages that express endogenous NRP2 ($P < 0.01$). The binding of HARS^{WHEP}-Fc to THP-1 macrophages, but not to monocytes, was in accordance with the up-regulation of surface NRP2 expression upon differentiation and polarization. Last, we showed that binding was blocked by either an a-HARS^{WHEP} antibody or an a-NRP2 antibody that specifically binds the b1 domain (Fig. 1H).

The b1 domain of NRP2 and “turn” of the HARS^{WHEP} HTH structure are responsible for the receptor-ligand interaction

Neuropilins are membrane proteins with a large 800–amino acid extracellular domain connected to a transmembrane helix and terminating in a C-terminal cytoplasmic tail of about 40 amino acids (40). Both NRP1 and NRP2 interact with semaphorin and vascular endothelial growth factor (VEGF) ligands. They are distinguished by the specificity of their interactions with these ligands. Both NRP1 and NRP2 have five extracellular domains, designated as a1, a2, b1, b2, and c. To map the domains of NRP2 that interact with HARS^{WHEP}-Fc, we first investigated binding interactions of individual, isolated NRP2 domains with HARS^{WHEP}-Fc using SPR. From these experiments, we found that the NRP2 a2b1b2 fragment interacted with HARS^{WHEP}-Fc, whereas the isolated b1 domain or b1b2 domains that could bind VEGF-C (fig. S1C) did not interact with HARS^{WHEP}-Fc ($P < 0.0001$; Fig. 1I).

We then took advantage of the interaction specificity of HARS^{WHEP}-Fc for NRP2 versus NRP1. This specificity enabled us to do domain-swap experiments using recombinant proteins to investigate the contribution of individual domains and also to maintain the context of the 3D structure. HARS^{WHEP}-Fc binding was analyzed by flow cytometry using Expi293 cells overexpressing the wild-type (WT) or domain-swapped NRP2 (fig. S1D). The cells were gated as the NRP2⁺ population, which showed comparable NRP2 surface expression across WT and domain swaps (fig. S1E). HARS^{WHEP}-Fc binding was reduced by the a2 ($P = 0.0019$), b1 ($P < 0.0001$), or b2 ($P < 0.0001$) domain swap in comparison with WT, whereas it was unaffected by the a1 domain swap

(Fig. 1J). These results demonstrate that the a2b1b2 domains but not the a1 domain of NRP2 provide the binding sites for HARS^{WHEP}-Fc. The b1 domain swap decreased the binding more than the a2 or b2 domain swap ($P < 0.01$), suggesting that the b1 domain is primarily responsible for the interaction with HARS^{WHEP}-Fc. The NRP2 a2b1b2 domains also encompass binding regions for the known NRP2 ligands VEGF and semaphorin. In a ligand-induced receptor dimerization assay, HARS^{WHEP}-Fc did not block VEGF-C or semaphorin 3F-induced NRP2/co-receptor dimerization (fig. S1F).

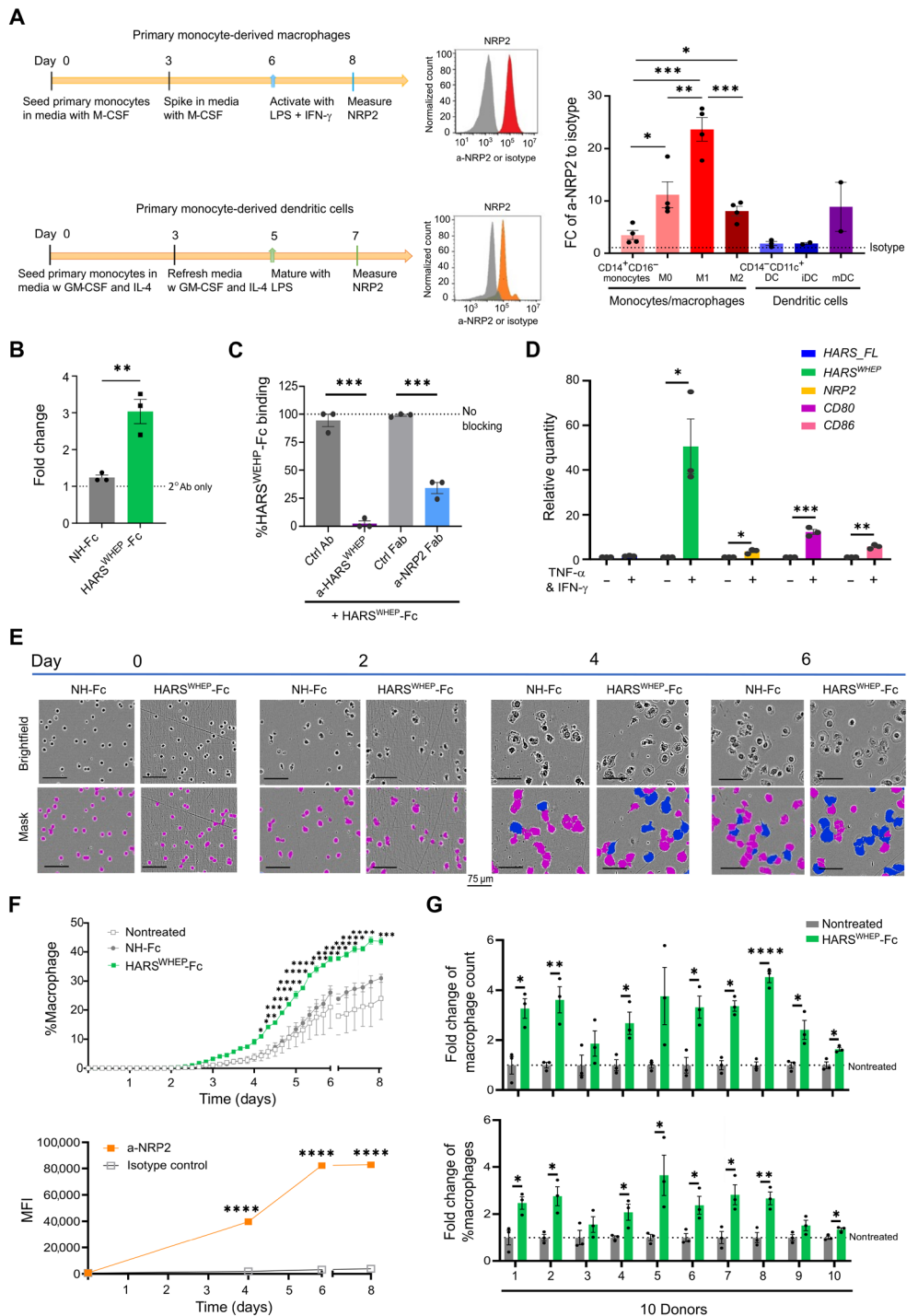
To further narrow down the inferred interaction site of HARS^{WHEP}-Fc with NRP2, we obtained crystals of HARS^{WHEP} with the antigen binding fragment (Fab) of the blocking a-HARS^{WHEP} antibody (fig. S1G). These crystals were of sufficient quality to obtain a 2.3-Å crystal structure (table S2). This cocrystal showed that residues in the turn and adjacent helices of the HARS^{WHEP} HTH interacted with the blocking antibody's Fab (Fig. 1K). Thus, we inferred that the middle loop of HARS^{WHEP} is critical to engage the interaction with NRP2 (fig. S1H). The amino acid sequences of the middle loop across different aaRS WHEP domains are poorly conserved (fig. S1I), and as expected, the interaction with NRP2 was specific to HARS^{WHEP} (fig. S1J).

HARS^{WHEP}-Fc binds to differentiated and stimulated macrophages enriched in NRP2

On the basis of the connection between HARS^{WHEP} and inflammation, we set out to better understand the regulation of NRP2 in primary immune cells. Immune cells were isolated from peripheral blood mononuclear cells (PBMCs) of healthy human donors and stained for NRP2 expression on naïve cells or cells stimulated by inflammatory cytokines or activating antibodies. NRP2 expression was relatively low on the surface of naïve monocytes, dendritic cells (DCs), and T cells as indicated by comparable staining signals of a-NRP2 and isotype control on these cells (Fig. 2A and fig. S2A). It was up-regulated specifically on myeloid cells such as macrophages upon induction of cell differentiation or stimulation with inflammatory agents. For example, M0 macrophages differentiated by macrophage colony-stimulating factor (M-CSF) showed more than a threefold increase in surface-localized NRP2 in comparison with unstimulated primary monocytes ($P = 0.0261$; Fig. 2A). By polarization of M0 macrophages to proinflammatory M1-like, NRP2 was further induced compared with M0 cells ($P = 0.0096$; Fig. 2A). In contrast, polarization to anti-inflammatory M2-like macrophages did not further increase NRP2 expression compared with M0 cells. In addition, stimulation of CD4⁺ and CD8⁺ T cells in the PBMCs from the same donors with a-CD3/a-CD28 failed to increase NRP2 expression (fig. S2A). Therefore, NRP2 was primarily induced on macrophages by differentiation and inflammatory stimulation, pointing to a potential role for this receptor in the inflammatory response.

Next, we demonstrated that HARS^{WHEP}-Fc bound to the cell surface of M0 macrophages with significantly more binding signal than the NH-Fc control protein by flow cytometry analysis ($P = 0.0059$; Fig. 2B). This binding was entirely blocked by the a-HARS^{WHEP} antibody (Fig. 1K) and inhibited by an a-NRP2 Fab that targets the b1 domain of NRP2 ($P < 0.001$; Fig. 2C). When the M0 macrophages were treated with the inflammatory cytokines TNF- α and IFN- γ , which induced HARS^{WHEP} expression in lung A549 cells (Fig. 1A), the macrophages also showed elevated HARS^{WHEP} expression compared with unstimulated cells ($P = 0.0155$; Fig. 2D and fig. S2B). In contrast, elevated expression was not observed for HARS_{FL} transcripts (Fig. 2D). Therefore, HARS^{WHEP} was induced by inflammatory stimulation

Fig. 2. Macrophages enriched in surface NRP2 expression were bound and modulated by HARS^{WHEP}-Fc. (A) Left: M0, M1-like, and M2-like macrophages or immature DCs (iDCs) and mature DCs (mDCs) were generated in vitro from primary CD14⁺CD16⁻ monocytes isolated from PBMCs, and NRP2 expression on the cell surface was evaluated by flow cytometry. Middle: representative histograms of NRP2 staining on M1 macrophages and mDCs. The x axis is a-NRP2 (red or orange) or isotype control (gray)—Alexa Fluor 647 fluorescence intensity—and the y axis is the normalized cell count. Right: NRP2 expression represented as fold change of a-NRP2 staining MFI relative to that of isotype control staining. For circulating monocytes and DCs, PBMCs were evaluated for NRP2 expression on monocyte (CD14⁺CD16⁻) and DC (CD14⁻CD11c⁺) populations. *n* = 4 donors for monocytes and macrophages, and *n* = 2 or 3 donors for DCs. Data are shown as mean ± SEM. **P* < 0.05, ***P* < 0.01, and ****P* < 0.001 by unpaired *t* test. (B) Fold change of a-Fc staining of bound HARS^{WHEP}-Fc (green) or NH-Fc control (gray) relative to that of secondary antibody-only staining on PMDMs measured by flow cytometry. Data are from three independent experiments. Two technical replicates were analyzed for each experiment, and means were used in the plot. Data are shown as mean ± SEM. ***P* < 0.01 by unpaired *t* test. (C) Percentage of HARS^{WHEP}-Fc binding on PMDMs in the presence of a-HARS^{WHEP} (purple), a-NRP2 Fab (blue), or isotype controls (gray) by flow cytometry analysis. Data are from three separate experiments. Two technical replicates were analyzed for each experiment, and means were used in the plot. Data are shown as mean ± SEM. ****P* < 0.001 by unpaired *t* test comparing a-HARS^{WHEP} or a-NRP2 Fab to the respective isotype control. (D) Relative quantity of mRNA expression for *HARS_FL*, *HARS^{WHEP}*, *NRP2*, *CD80*, and *CD86* in cytokine-treated PMDMs to that for the vehicle-treated control. PMDMs were analyzed 68 hours posttreatment by TNF-α and IFN-γ or vehicle control. Up-regulation of *CD80* and *CD86* served as positive controls to indicate PMDM activation. Two separate experiments were performed. Shown are representative data with *n* = 3 biological replicates. Data are shown as mean ± SEM. **P* < 0.05, ***P* < 0.01, and ****P* < 0.001 by unpaired *t* test. (E) Representative images are shown for monocyte and macrophage-like cells with HARS^{WHEP}-Fc or NH-Fc treatment of PMDMs at day 0, 2, 4, and 6 post-cell seeding and treatment. Primary monocytes from a healthy donor were differentiated by M-CSF in the presence or absence of HARS^{WHEP}-Fc or NH-Fc. Pink: mask for cells with monocyte-like morphology, and blue: mask for cells with macrophage-like morphology. Scale bars, 75 μm. Quantification results are shown in (F) and (G). (F) Top: kinetic plot of percentage of PMDMs with macrophage-like morphology during 8 days of culture in the presence of M-CSF, with or without HARS^{WHEP}-Fc (green) or NH-Fc (gray) treatment. Bottom: a-NRP2 (yellow) versus isotype control (black) staining of PMDMs during 8 days of culture in the presence of M-CSF only. Three separate experiments were performed. Shown are representative data with *n* = 3 biological replicates for macrophage percentage and *n* = 3 technical replicates for staining of NRP2 expression. Data are shown as mean ± SEM. **P* < 0.05, ***P* < 0.01, ****P* < 0.001, and *****P* < 0.0001 significantly different between HARS^{WHEP}-Fc and NH-Fc treatment or a-NRP2 and isotype control staining at a specific time point by two-way ANOVA followed by Tukey's multiple group comparisons test. (G) Fold change of HARS^{WHEP}-Fc (green) over nontreated control (gray) in area under the curve of macrophage count or percentage macrophage plots from days 0 to 4 in PMDMs. Data are shown as mean ± SEM. **P* < 0.05, ***P* < 0.01, and *****P* < 0.0001 significantly different between HARS^{WHEP}-Fc and nontreated by unpaired *t* test for each donor. GM-CSF, granulocyte-macrophage colony-stimulating factor.



of both lung and macrophage cells and may act on macrophages in a paracrine or autocrine manner through NRP2.

HARS^{WHEP}-Fc down-regulates a key inflammatory receptor and cytokines in primary monocyte-derived macrophages

To explore the functional impact of the binding of HARS^{WHEP}-Fc to myeloid cells, we isolated primary CD14⁺CD16⁻ monocytes from healthy human donors. These cells were then differentiated into macrophages by M-CSF in the presence or absence of HARS^{WHEP}-Fc. They were then evaluated for morphological change, transcriptional regulation, cell surface marker expression, as well as cytokine expression and secretion. HARS^{WHEP}-Fc promoted an unexpected morphology change across the differentiation of primary monocyte-derived macrophages (PMDMs). With HARS^{WHEP}-Fc treatment, the number and percentage of cells with macrophage morphology were increased when compared with cells treated with the control protein NH-Fc or nontreated ($P < 0.05$; Fig. 2, E and F), and this effect was entirely blocked by an a-HARS^{WHEP} Fab (fig. S3). In a time-course study, the increase in percentage of macrophages aligned with NRP2 up-regulation on the surface of these cells ($P < 0.0001$; Fig. 2F), consistent with a correlation between NRP2 expression and appearance of macrophages as well as an effect by HARS^{WHEP}-Fc through binding to NRP2. These observations were consistent across a total of 10 tested donors (Fig. 2G).

The subsequent high-throughput whole-transcriptome sequencing [RNA sequencing (RNA-seq)] showed that HARS^{WHEP}-Fc-treated PMDMs had distinct transcriptional profiles compared with the NH-Fc-treated or nontreated cells by principal components analysis (PCA; Fig. 3A). Through UCSD (University of California San Diego) gene set enrichment analysis (GSEA) of the 50 hallmark gene sets that represent specific, well-defined biological states or events, the PMDMs from two donors had the same 11 gene sets down-regulated by HARS^{WHEP}-Fc [$P < 0.05$ and false discovery rate (FDR) q value < 0.2 ; Fig. 3B and table S4]. These include immunoregulatory gene sets such as TNFa_signaling_via_NFkB, allograft_rejection, inflammatory_response, and IL2_STAT5_signaling.

HARS^{WHEP}-Fc inhibited the gene expression or secretion of a wide array of inflammatory cytokines including MCP-1 (encoded by *CCL2*), TNF- α , IFN- γ , and interleukins compared with NH-Fc control by RNA-seq and Meso Scale Diagnostics (MSD) analyses ($P < 0.05$; Fig. 3, C and D). Investigation of common macrophage markers (classically activated, alternatively activated, or fibrotic) showed that HARS^{WHEP}-Fc also reduced gene expression and the surface amount of CD14, a co-receptor of Toll-like receptor 4 (TLR4) for inflammatory signaling, compared with NH-Fc control ($P < 0.001$; Fig. 3, C and E, and table S5). These results were consistent across both human donors. Other markers such as CD80 and CD86 (classically activated or M1 markers) and CD163 and CD206 (alternatively activated or M2 markers) showed nonsignificant or nonconsistent changes in the two donors (table S5). These results together with the transcriptional profiling data suggested that HARS^{WHEP}-Fc did not drive macrophages toward the M1-like or M2-like subtype but instead modulated them to manifest a distinct, less inflammatory profile with reduced expression of surface receptor and proinflammatory cytokines. In further analysis, we found that *MYC* mRNA expression and pathways related to the cell cycle (G2M_checkpoint and E2F_targets) were also down-regulated by HARS^{WHEP}-Fc versus NH-Fc treatment of PMDMs ($P < 0.05$; Fig. 3B and fig. S4), thereby indicating that cell proliferation was inhibited.

HARS^{WHEP}-Fc inhibits inflammation and fibrosis across preclinical models of ILDs

Early studies into the potential mechanism of HARS^{WHEP}-Fc sought to understand its possible role in trafficking of immune cells using an LPS acute lung inflammation model. These studies demonstrated that systemic delivery of HARS^{WHEP}-Fc reduced infiltration of myeloid cells (in particular alveolar macrophages, inflammatory monocytes, DCs, and neutrophils) into bronchoalveolar lavage and lung tissue samples from mice (31). Building on these initial findings that HARS^{WHEP}-Fc can affect immune cell trafficking to the lung, we aimed to further evaluate its potential efficacy in a standard model of lung injury characterized by chronic inflammation and fibrosis. In a mouse model of bleomycin-induced pulmonary fibrosis, treatment of bleomycin-induced animals with HARS^{WHEP}-Fc (0.4 mg/kg on days 8 and 15 of post-bleomycin instillation) led to a significant reduction in lung fibrosis as determined by Ashcroft scoring ($P = 0.0015$) in comparison with animals dosed with vehicle (Fig. 4A). Inflammation scores trended lower in the HARS^{WHEP}-Fc-treated group but were not statistically significantly different from the vehicle group.

In addition, HARS^{WHEP}-Fc was evaluated head-to-head with nintedanib in a rat model of bleomycin-induced lung fibrosis. In the rat, HARS^{WHEP}-Fc was administered on days 2, 9, and 16 after the first bleomycin dose and attenuated deleterious Ashcroft scores significantly ($P = 0.037$) when compared with its matched vehicle control (Fig. 4B). The inflammation scores were significantly lower in the HARS^{WHEP}-Fc group when comparing with the nintedanib vehicle group but not the HARS^{WHEP}-Fc vehicle group ($P = 0.0408$; Fig. 4B). Analyses of lung hydroxyproline content and respiratory minute volume assessment were also performed in the rat bleomycin study, which demonstrated a significant improvement in respiratory function when comparing the HARS^{WHEP}-Fc group with the HARS^{WHEP}-Fc vehicle group ($P = 0.0017$; fig. S5). Nintedanib, which was dosed daily from day 9 through day 22 after the initial bleomycin dose, did not alter any of the analyzed end points in this study (Fig. 4B and fig. S5).

To expand upon these findings and increase confidence in the therapeutic activity of HARS^{WHEP}-Fc, we evaluated it across a panel of preclinical mouse models of ILD. These included mouse models that induce inflammatory lung responses including a model of silicosis induced by silica; a model of CHP induced by the bacterium *Saccharopolyspora rectivirgula*; a model of sarcoidosis induced by the bacterium *Propionibacterium acnes*; a model of rheumatoid arthritis (RA)-ILD developed in BALB/c-Zap70*W163C (SKG) mice, which spontaneously develop chronic autoimmune arthritis; and a mouse model of SSc induced as part of a chronic graft-versus-host disease (cGvHD) response to a bone marrow transplant (Fig. 4, C to G). End-point analysis for all models included histological analysis of the lung as well as expression of the inflammatory biomarkers IFN- γ , interleukin-6 (IL-6), and MCP-1 in the lung tissue.

In the murine silicosis model, HARS^{WHEP}-Fc treatment produced a statistically significant reduction in the collagen content in the lung ($P = 0.0489$) and lowered the amount of IFN- γ expressed in the lung ($P = 0.0187$) compared with the vehicle control group (Fig. 4C). Histopathological end points such as Ashcroft scores or inflammation scores were not changed by HARS^{WHEP}-Fc treatment in this study (Fig. 4C).

In the *S. rectivirgula* model of CHP, the histological end points determining the pneumonia score or bronchus-associated lymphoid tissue (BALT) area were not changed in the HARS^{WHEP}-Fc group

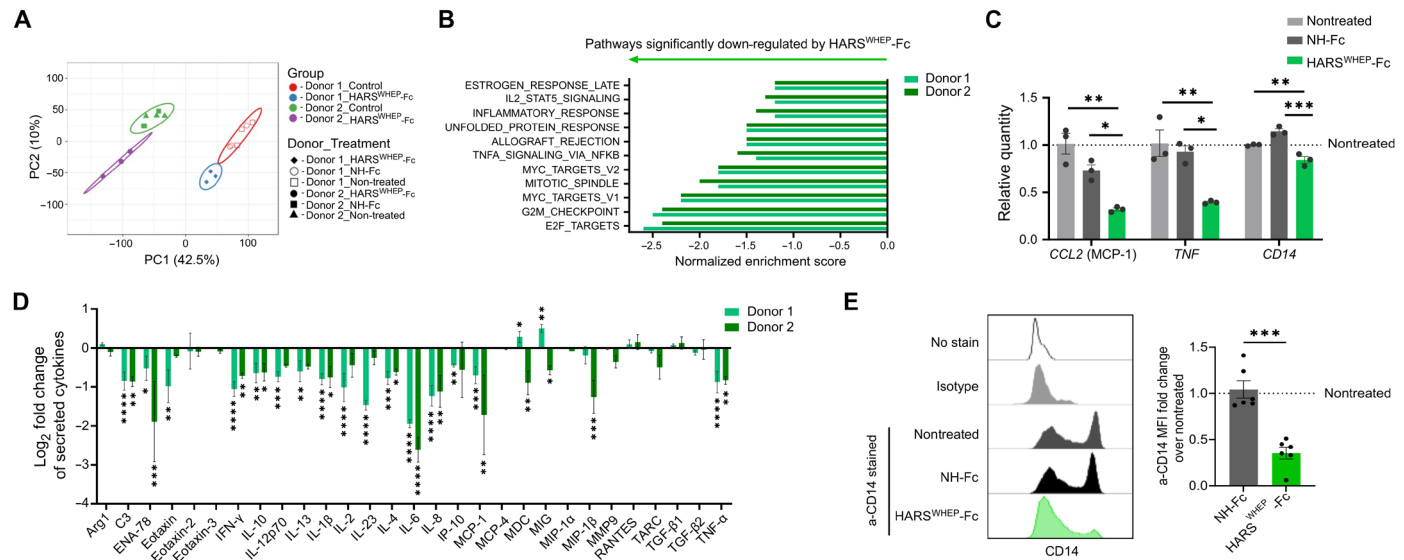


Fig. 3. HARS^{WHEP}-Fc down-regulated inflammatory pathways, cytokines, and CD14 receptor in PMDMs. (A) PCA plot for transcriptomes of PMDMs treated with HARS^{WHEP}-Fc, NH-Fc, or nontreated. Cells from two donors were used in this study. For each donor, $n = 3$ biological replicates for each treatment. In group clustering, $n = 3$ for the HARS^{WHEP}-Fc group, and $n = 6$ for the control group (three of NH-Fc and three of nontreated). (B) Normalized enrichment scores (NESs) of hallmark gene sets comparing the transcriptomes of PMDMs treated with HARS^{WHEP}-Fc versus control by GSEA. $n = 3$ for HARS^{WHEP}-Fc, and $n = 6$ for control (three of NH-Fc and three of nontreated) for each donor. A total of 50 hallmark gene sets were analyzed, and shown are those significantly down-regulated (with negative NESs) by HARS^{WHEP}-Fc treatment in comparison with control (NH-Fc and nontreated) in both donors. Significance was calculated by GSEA and defined as normalized $P < 0.05$ and normalized FDR q value < 0.2 . (C) Relative quantity of *CCL2* (encoding MCP-1), *TNF*, or *CD14* mRNA expression in HARS^{WHEP}-Fc (green)– or NH-Fc (dark gray)–treated PMDMs to that in nontreated cells (light gray) based on the RNA-seq data analysis. $n = 3$ biological replicates. Data are shown as mean \pm SEM. * $P < 0.05$, ** $P < 0.01$, and *** $P < 0.001$ by one-way ANOVA followed by Tukey's multiple group comparisons test. (D) Shown are log₂(fold change) of secreted cytokine quantities from PMDMs with HARS^{WHEP}-Fc treatment compared with NH-Fc control by MSD cytokine assays of culture supernatants. Cells from two donors were used in this study. For each donor, two independent experiments were performed; $n = 4$ biological replicates. Data are shown as mean \pm SEM. P values for comparing fold changes of HARS^{WHEP}-Fc and NH-Fc groups in each cytokine secretion were derived from two-way ANOVA followed by Tukey's multiple group comparisons test. * $P < 0.05$, ** $P < 0.01$, *** $P < 0.001$, and **** $P < 0.0001$. (E) Cell surface CD14 receptor expression in HARS^{WHEP}-Fc– or NH-Fc–treated PMDMs by flow cytometry analysis. Left: representative flow spectra of PMDMs with no stain, isotype control, or a-CD14 staining. Right: fold change of a-CD14 staining MFI in NH-Fc (gray)– or HARS^{WHEP}-Fc (green)–treated cells relative to that in nontreated cells. Cells from six donors were used in this study. Two technical replicates were analyzed for the experiment with each donor, and the means were used in the plot. Data are shown as mean \pm SEM. *** $P < 0.001$ by unpaired t test.

(Fig. 4D). The inflammatory markers IFN- γ ($P = 0.0251$) and MCP-1 ($P = 0.0008$) were significantly lower in the animals treated with HARS^{WHEP}-Fc (Fig. 4D).

Similar to the CHP model, no changes in histological end points were produced by HARS^{WHEP}-Fc treatment in the *P. acnes* model (Fig. 4E) compared to the control group. However, all three markers, IFN- γ ($P = 0.0346$), IL-6 ($P = 0.0021$), and MCP-1 ($P = 0.0247$), were reduced in a significant manner compared with vehicle control (Fig. 4E).

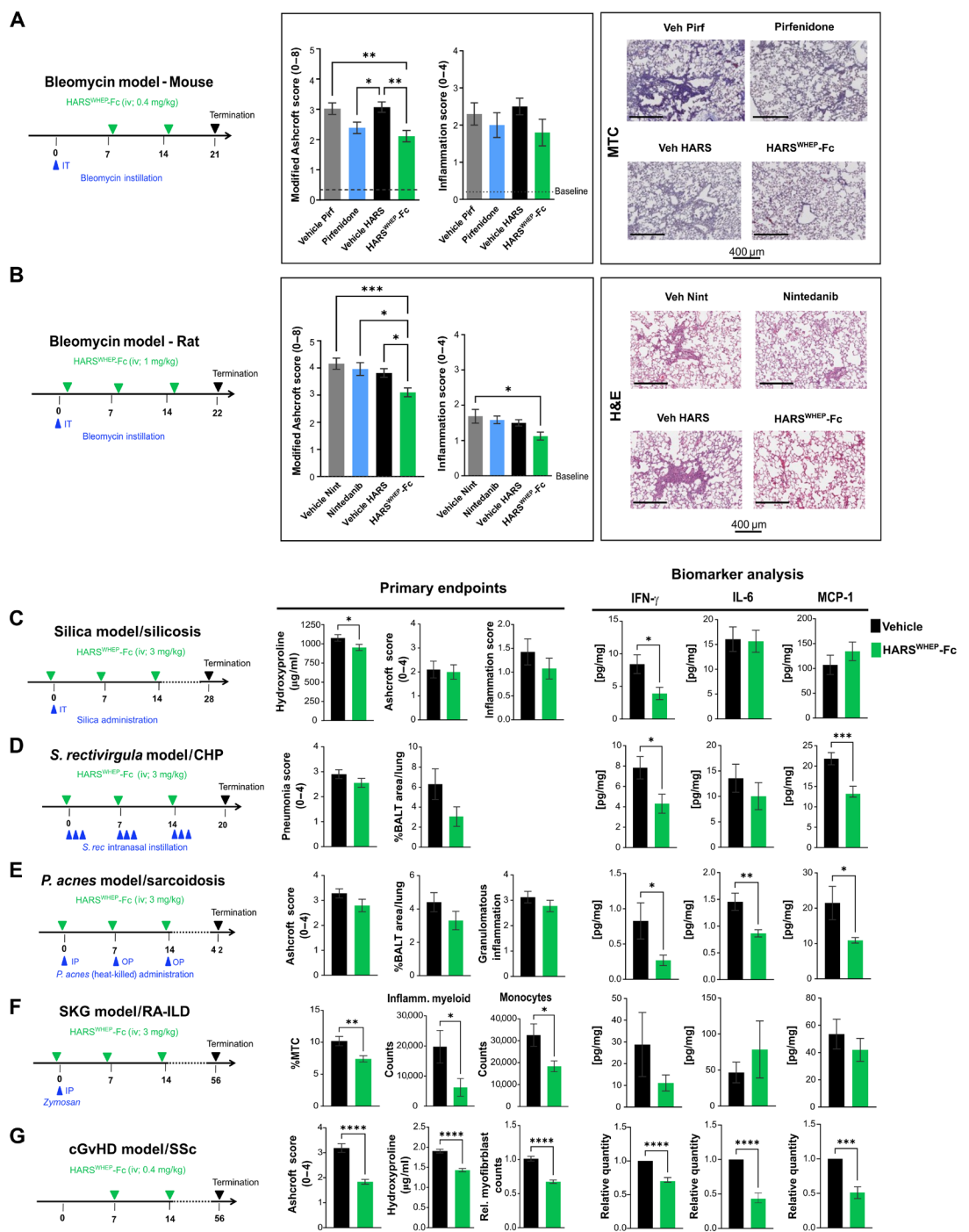
Compared with vehicle control, HARS^{WHEP}-Fc produced a statistically significant reduction in lung fibrosis in the SKG mouse model of RA-ILD as demonstrated by reduced Masson's trichrome (MTC) staining ($P = 0.0092$; Fig 4F). In addition, a strong reduction in inflammatory myeloid cells ($P = 0.0467$) and monocytes ($P = 0.0455$) was achieved with HARS^{WHEP}-Fc treatment (Fig. 4F).

Last, in the sclerodermatous cGvHD mouse model, Ashcroft scores ($P < 0.0001$), amount of hydroxyproline ($P < 0.0001$), and myofibroblast counts ($P < 0.0001$) were reduced in response to HARS^{WHEP}-Fc treatment as compared with the vehicle control (Fig. 4G). RNA isolated from the lungs showed significant down-regulation of *IFNG* ($P < 0.0001$), *IL6* ($P < 0.0001$), and *CCL2* (encoding MCP-1; $P = 0.0007$) transcripts in response to HARS^{WHEP}-Fc relative to the vehicle control group (Fig. 4G).

NRP2 is enriched on myeloid cells in affected tissues from patients with inflammatory ILD

To better understand the expression of NRP2, the target receptor of HARS^{WHEP}-Fc, in the affected tissues of patients with inflammatory ILD and confirm its up-regulation on myeloid cells in sites of chronic inflammation, we performed an extensive analysis of NRP2 expression in patient biopsy samples. In previous work, we discovered that NRP2 protein was enriched in sarcoidosis granulomas [clumps of inflammatory cells found in one or more organs of the body denoted by the presence of Langhans giant cells, which are myeloid in nature (41)] found in tissue biopsies from patients with sarcoidosis by immunohistochemistry (IHC) (31, 42). In the current work, we expanded the analysis to a related form of ILD and detected NRP2 expression in the affected skin of patients with SSc by IHC (Fig. 5A and fig. S6). Moreover, using a specific in situ costaining hybridization technique, we were able to detect colocalization of NRP2 RNA with macrophage markers CD68 and CD163. In lung biopsies from four patients with pulmonary sarcoidosis, NRP2 was significantly more colocalized with CD68⁺ and CD163⁺ macrophages than with CD4⁺ and CD8⁺ T cells ($P < 0.05$; Fig. 5B). Consistently, high percentages of colocalization of NRP2 and macrophage markers were observed in the skin biopsies of five patients with SSc (Fig. 5C). NRP2 was expressed at a higher amount on circulating monocytes

Fig. 4. HARS^{WHEP}-Fc reduced inflammation and fibrosis in pre-clinical models of ILD. (A) Shown is the HARS^{WHEP}-Fc dosing regimen and timeline (days) of the mouse lung bleomycin model (left). iv, intravenous; IT, intratracheal. Ashcroft scores and inflammation scores are shown for pirfenidone, HARS^{WHEP}-Fc, and their respective vehicle controls (middle). Representative MTC-stained images of each of the treatment groups are shown (right). Pirfenidone served as a positive control in this model. *n* = 10 for each group. A dotted line in the graphs indicates the baseline amounts from healthy mice. Data are shown as mean ± SEM. **P* < 0.05 and ***P* < 0.01 by one-way ANOVA followed by Tukey's multiple group comparisons test. **(B)** Shown is the HARS^{WHEP}-Fc dosing regimen and timeline of the rat lung bleomycin model (left). Ashcroft scores and inflammation scores are shown for nintedanib, HARS^{WHEP}-Fc, and their respective vehicle controls (middle). Representative H&E-stained images of each of the treatment groups are shown (right). Nintedanib served as a positive control in this model. *n* = 8 for each group. Data are shown as mean ± SEM. A dotted line in the graphs indicates the baseline amounts from healthy mice. **P* < 0.05 and ****P* < 0.001 by one-way ANOVA followed by Tukey's multiple group comparisons test. **(C)** Shown is the HARS^{WHEP}-Fc dosing regimen and timeline of the mouse silica model (left). Lung collagen content, Ashcroft scores, and inflammation scores are shown for HARS^{WHEP}-Fc and its vehicle control (middle). Lung homogenates were analyzed for IFN-γ, IL-6, and MCP-1 expression using a multiplex ELISA (right). *n* = 10 for each group. Data are shown as mean ± SEM. **P* < 0.05 and ****P* < 0.001 by unpaired *t* test. **(D)** Shown is the HARS^{WHEP}-Fc dosing regimen and timeline of the murine CHP model (left). Pneumonia scores and %BALT area/lung are shown for HARS^{WHEP}-Fc and its vehicle control (middle). Lung homogenates were analyzed for IFN-γ, IL-6, and MCP-1 expression using a multiplex ELISA (right). *n* = 10 for each group. Data are shown as mean ± SEM. **P* < 0.05 and ****P* < 0.001 by unpaired *t* test. **(E)** Shown is the HARS^{WHEP}-Fc dosing regimen and timeline of the murine sarcoidosis model (left). IP, intraperitoneal; OP, oropharyngeal. Ashcroft scores, %BALT area/lung, and granulomatous inflammation scores are shown for HARS^{WHEP}-Fc and its vehicle control (middle). Lung homogenates were analyzed for IFN-γ, IL-6, and MCP-1 expression using a multiplex ELISA (right). *n* = 8 for vehicle, and *n* = 10 for HARS^{WHEP}-Fc. Data are shown as mean ± SEM. **P* < 0.05 and ****P* < 0.01 by unpaired *t* test. **(F)** Shown is the HARS^{WHEP}-Fc dosing regimen and timeline of the murine RA-ILD model (left). %MTC per lung section and immune cell counts (inflammatory myeloid cells and monocytes) from lung single-cell suspensions are shown for HARS^{WHEP}-Fc and its vehicle control (middle). Lung homogenates were analyzed for IFN-γ, IL-6, and MCP-1 expression using a multiplex ELISA (right). *n* = 9 or 10 for vehicle and *n* = 7 or 8 for HARS^{WHEP}-Fc depending on the end point. Data are shown as mean ± SEM. **P* < 0.05 and ***P* < 0.01 by unpaired *t* test. **(G)** Shown is the HARS^{WHEP}-Fc dosing regimen and timeline of the murine SSc model (left). Ashcroft scores, hydroxyproline content, and myofibroblast counts are shown for HARS^{WHEP}-Fc and its vehicle control (middle). RNA extracted from the lung was analyzed for *IFNG*, *IL6*, and *CCL2* (MCP-1) transcript quantities by quantitative polymerase chain reaction (right). *n* = 8 for each group. Data are shown as mean ± SEM. ****P* < 0.001 and *****P* < 0.0001 by unpaired *t* test.



Downloaded from https://www.science.org at Scripps Research Institute on March 12, 2025

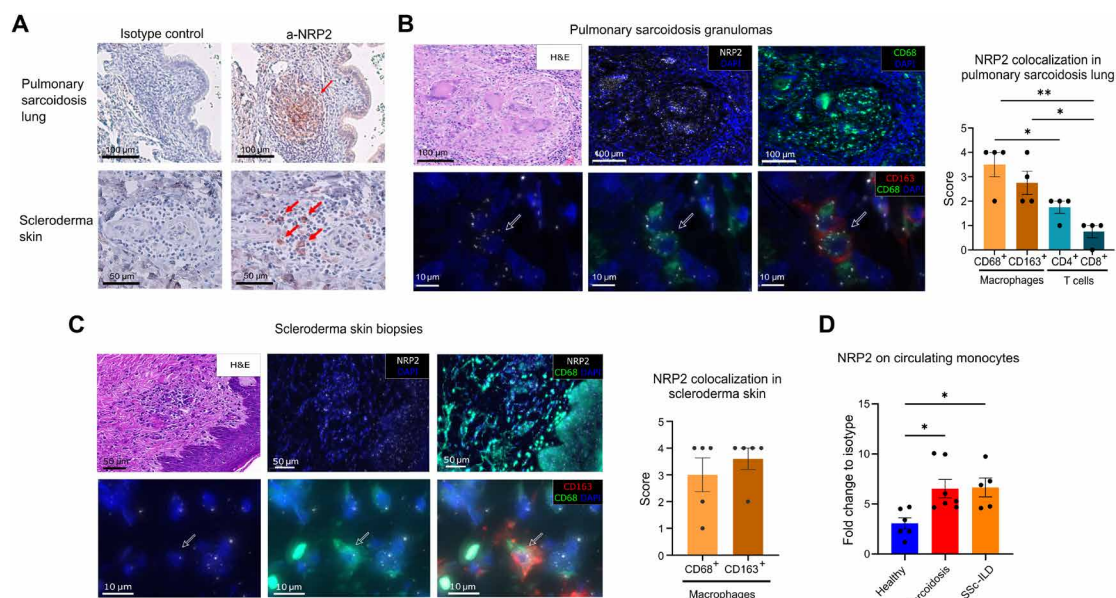


Fig. 5. NRP2 was expressed on myeloid cells of human disease samples. (A) IHC staining is shown for human pulmonary sarcoidosis lung and scleroderma skin tissue with isotype control or a-NRP2 antibody (see also fig. S6). Red arrows indicate NRP2 reactivity. Scale bars, 100 μ m for pulmonary sarcoidosis lung and 50 μ m for scleroderma skin. (B) Left: RNAScope staining of NRP2 (white) and IF staining of myeloid cell markers CD68 (green) and CD163 (red). DAPI stains the nuclei (blue). Arrows indicate colocalization of NRP2 with macrophage markers. Scale bars, 100 μ m for top images and 10 μ m for bottom images. Right: semiquantification of NRP2 colocalization with macrophage or T cell markers in four biopsies from distinct patients with pulmonary sarcoidosis. See table S9 for sample information. Data are shown as mean \pm SEM. $*P < 0.05$ and $**P < 0.01$ by one-way ANOVA followed by Tukey's multiple group comparisons test. (C) Left: RNAScope staining of NRP2 (white) and IF staining of macrophage markers CD68 (green) and CD163 (red). DAPI stains the nuclei (blue). Arrows indicate colocalization of NRP2 with macrophage markers. Scale bars, 50 μ m for top images and 10 μ m for bottom images. Right: semiquantification of NRP2 colocalization with macrophage markers in five biopsies from distinct patients with SSc. See table S9 for sample information. Data are shown as mean \pm SEM. No statistical significance was found by unpaired *t* test. (D) NRP2 expression on CD14⁺ monocytes from healthy donors and patients with ILDs, represented as fold change of a-NRP2 staining MFI relative to that of isotype control staining. $n = 5$ to 7 for each group. Data are shown as mean \pm SEM. $*P < 0.05$ by one-way ANOVA followed by Dunnett's group comparisons using the healthy donor group as control.

in patients with sarcoidosis and SSc-ILD compared with healthy controls ($P < 0.05$; Fig. 5D). Collectively, these results indicated that NRP2 was highly expressed on circulating monocytes and macrophages in affected tissues of patients with ILDs.

Given the high amounts of NRP2 expression observed in myeloid cells from patients with ILDs, we wanted to explore whether cells from these patients would behave in a similar or different manner to healthy individuals when differentiated in the presence of HARS^{WHEP}-Fc. Despite difficulty in obtaining PBMC samples from patients with ILDs with sufficient cell numbers to support in vitro mechanistic studies, we were able to obtain cells from two patients with sarcoidosis to explore the morphology change or transcriptome profile. Consistent with the observations in healthy individuals, HARS^{WHEP}-Fc promoted differentiation of patient PMDMs, increasing the percentage and count of cells with macrophage morphology in comparison with NH-Fc or nontreated control ($P < 0.0001$; fig. S7A). From one patient, the PMDM number was sufficient for transcriptome profiling by RNA-seq followed by GSEA. Among the 50 analyzed hallmark gene sets, 14 gene sets (including immunoregulatory, EMT, and cell cycle pathways) were down-regulated by HARS^{WHEP}-Fc versus control ($P < 0.05$ and FDR q value < 0.2 ; table S6). The top three down-regulated pathways were all immune related including inflammatory response, allograft rejection, and TNF α signaling via NF κ B (Fig. 6A). These were also among gene sets down-regulated by HARS^{WHEP}-Fc in PMDMs from two healthy donors but were ranked higher in patient cells with more negative enrichment scores (-1.9 to -1.7 in the patient and -1.5 to -1.2 in

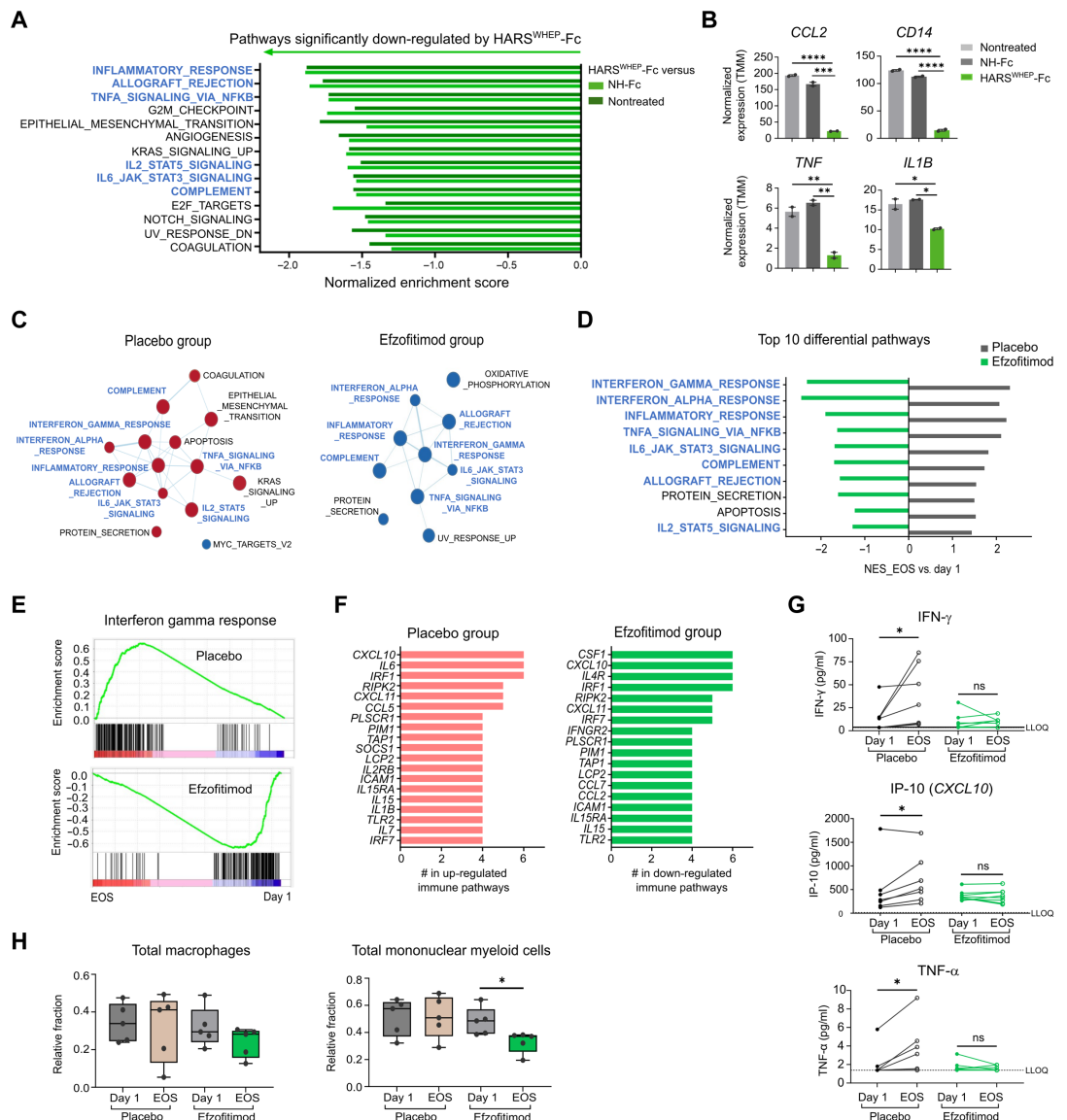
the healthy donors). Gene expressions of inflammatory cytokines and receptor (*CCL2*, *TNF*, and *CD14*) were also reduced to a greater extent by HARS^{WHEP}-Fc in cells from the patient with sarcoidosis compared with the healthy donor ($P < 0.01$; Fig. 6B and fig. S7B). It was also noted that the nontreated patient PMDMs had a much higher *CCL2* and *TNF* expression compared with that of healthy donors ($P < 0.001$; fig. S7C).

Efzofitimid treatment down-regulates inflammatory biomarkers and pathways in circulating PBMCs from patients with sarcoidosis

HARS^{WHEP}-Fc completed a phase 1b/2a clinical trial for treatment of patients with sarcoidosis with a good manufacturing practice (GMP)-manufactured version (international nonproprietary name: efzofitimid). The clinical trial and results were described in detail previously (31–33). The data generated by this trial provided the opportunity to examine biomarkers in patients with sarcoidosis with efzofitimid or placebo treatment. These patients were receiving palliative steroid therapy (prednisone). In a 24-week course of study, the patients were treated with efzofitimid or placebo, and steroids were tapered down during the first 8 weeks (fig. S8A). RNA-seq was performed on PBMCs of patients using samples collected on day 1 before the treatment of placebo or efzofitimid as baseline and those collected at the end of study (EOS; week 24) posttreatment. The PCA of the RNA-seq data suggested that the efzofitimid and placebo groups at EOS had more distinct transcriptome profiles compared with baseline,

Fig. 6. HARS^{WHEP}-Fc (efzoftimod) down-regulated inflammatory pathways and biomarkers in immune cells from patients with sarcoidosis.

(A) NES of hallmark gene sets comparing the transcriptome of patient PMDMs treated with HARS^{WHEP}-Fc versus NH-Fc (light green) or nontreated (dark green) by GSEA. Cells from a patient with sarcoidosis were used in this study. Because of the limited cell number, cells were pooled from 10 96-well plates for each treatment condition for RNA extraction. *n* = 2 technical replicates in the RNA-seq experiment. A total of 50 hallmark gene sets were analyzed, and shown are those significantly down-regulated by HARS^{WHEP}-Fc treatment in comparison with NH-Fc or nontreated. Significance was calculated by GSEA and defined as normalized *P* < 0.05 and normalized FDR *q* value < 0.2. Pathways directly related to immune responses are labeled in blue. **(B)** Gene expression of the inflammatory cytokines *CCL2*, *TNF*, and *IL1B* and receptor *CD14* in patient PMDMs by RNA-seq analysis. Shown are normalized counts in trimmed mean of M values (TMM). PMDM treatment was the same as described in (A). *n* = 2 technical replicates. Data are shown as mean ± SEM. **P* < 0.05, ***P* < 0.01, ****P* < 0.001, and *****P* < 0.0001 by one-way ANOVA followed by Tukey's multiple group comparisons test. **(C)** Pathway networks showing the transcriptome changes in PBMCs in placebo and efzoftimod-treated patients at EOS (posttreatment; week 24) compared with day 1 of study (pretreatment; see also fig. S8A). Red nodes indicate up-regulation, and blue nodes indicate down-regulation at EOS versus day 1. PBMCs from patients with sarcoidosis before and after treatment by placebo or efzoftimod were used in this study. *n* = 5 patients in each group for the RNA-seq data analysis. A total of 50 hallmark gene sets were analyzed by GSEA, and shown are significantly enriched ones by Cytoscape network analysis and visualization. Significance was calculated by GSEA, and the Cytoscape visualization cutoff was defined as normalized *P* < 0.01 and normalized FDR *q* value < 0.2. Pathways directly related to immune responses are labeled in blue. **(D)** NES of hallmark gene sets comparing the transcriptomes of PBMCs from placebo or efzoftimod-treated patients at EOS versus day 1. *n* = 5 patients in each group. A total of 50 hallmark gene sets were analyzed by GSEA and ranked by ΔNES (placebo-efzoftimod). Shown are the top 10 pathways in ΔNES between the placebo and efzoftimod groups, and those directly related to immune responses are labeled in blue. **(E)** NES plots for the gene set of IFN-γ response comparing EOS versus day 1 for the efzoftimod and placebo groups. The top plot shows the running enrichment score for the gene set as the analysis walked down the ranked gene list by GSEA of RNA-seq data. The bottom plot shows where the markers of the gene set appear in the ranked gene list. Red indicates markers enriched at EOS compared with day 1, and blue indicates those enriched at day 1 compared with EOS. See also fig. S8D for the NES plots for the gene sets of interferon-α response and inflammatory response. **(F)** Core enriched genes in the placebo and in the efzoftimod groups by the GSEA leading edge analysis. Genes are ranked on the basis of how many times (#) they are included in the immune pathways significantly up-regulated (for the placebo group) or down-regulated (for the efzoftimod group) comparing transcriptomes at EOS versus day 1. Significance was calculated by GSEA and defined as normalized *P* < 0.05 and normalized FDR *q* value < 0.2. **(G)** Biomarker serum amounts on day 1 and EOS for each patient with sarcoidosis in the placebo and efzoftimod treatment groups (see also fig. S8E for plots of fold change for EOS relative to day 1 and IL-6 and MCP-1 data). *n* = 7 for the placebo group, and *n* = 8 for the efzoftimod group. Data are shown as line plots for serum amounts before and after treatment. LLOQ, lower limit of quantification. **P* < 0.05 by paired *t* test (Wilcoxon matched-pairs signed-rank test). ns means nonsignificant. **(H)** Relative fractions of total macrophages and total mononuclear myeloid cells in the placebo and efzoftimod groups before and after treatment as estimated by CIBERSORTx deconvolution analysis using the transcriptome data described in (C). Total macrophages include M0, M1-like, and M2-like. Total mononuclear myeloid cells include macrophages, monocytes, and DCs. See also fig. S8F for relative fractions of all 22 immune cell types and fig. S8G for relative fractions of grouped cell subsets and individual mononuclear myeloid cell types. *n* = 5 patients in each group. Data are shown in a box-and-whisker plot. The box represents the interquartile range. The line within the box indicates the median value. The whiskers show the minimum and maximum values within the dataset. **P* < 0.05 by unpaired *t* test.



Downloaded from https://www.science.org at Scripps Research Institute on March 12, 2025

indicating a differential effect of efzofitimod and placebo on the patients (fig. S8B). Specifically, whereas the placebo group showed up-regulation of multiple immune pathways, which we assume was a result of steroid tapering, efzofitimod treatment significantly reduced these pathways ($P < 0.05$ and FDR q value < 0.2 by GSEA; Fig. 6C, fig. S8C, and table S7).

Multiple immune pathways were among the top 10 differentially regulated pathways between placebo and efzofitimod-treated patients. The top gene sets were for *interferon_gamma_response*, *interferon_alpha_response*, and *inflammatory_response* (Fig. 6, D and E, and fig. S8D). The leading edge analysis of core enriched genes in the immune pathways revealed that genes including *CXCL10*, *CXCL11*, and *IRF7*, which are involved in IFN signaling, were up-regulated in the placebo group and also overlapped with ones down-regulated in the efzofitimod group (Fig. 6F). Consistent with the gene expression data, serum amounts of inflammatory biomarkers for sarcoidosis such as IFN- γ , IP-10 (interferon-gamma inducible protein 10, encoded by *CXCL10*), and TNF- α increased in the placebo group at EOS versus the baseline at day 1 ($P < 0.05$; Fig. 6G). In contrast, these markers showed no increase at EOS compared to day 1 in the efzofitimod group (Fig. 6G) and were significantly lower in the fold change of EOS versus day 1 compared to the placebo group ($P < 0.05$; fig. S8E). Relative fractions of 22 immune cell subsets in the patient PBMCs were further estimated by deconvolution of the bulk RNA-seq data using CIBERSORTx, a computational method for quantifying cell fractions (43). A decrease in the fraction of total mononuclear myeloid cells, including monocytes, macrophages, and DCs, was observed in the efzofitimod-treated group ($P = 0.0309$) but not in the placebo group comparing EOS and day 1 (Fig. 6H). Other cell subsets such as B, T, and natural killer cells showed comparable results between efzofitimod and placebo groups (fig. S8, F and G). This finding is consistent with the myeloid-relevant mechanism of action for efzofitimod's efficacy in reducing inflammation. Together, these results demonstrate that efzofitimod better controlled inflammation in the patients with sarcoidosis during steroid tapering. Figure S9 illustrates efzofitimod's mechanism of action on myeloid cells and the impact on patients with sarcoidosis on the basis of findings from this study.

DISCUSSION

Sarcoidosis and connective tissue diseases such as SSc are a heterogeneous group of systemic inflammatory disorders (41, 44). The development of ILD associated with these diseases is a key complication associated with morbidity and mortality. However, therapeutic options for ILD are limited, and new therapeutic targets or modalities are in demand for better disease management (45). In the airway and lung microenvironment, myeloid cells such as alveolar, interstitial, and monocyte-derived macrophages play key roles in homeostatic regulation as well as during the development of inflammation and fibrosis in individuals with ILDs (46). As such, modulation of myeloid cells may represent a therapeutic strategy for inflammatory and fibrosing lung diseases. The therapeutic form of HARS^{WHEP}, which showed immunomodulatory functions on macrophages through the binding to NRP2, reduced lung inflammation and fibrosis in multiple animal models of ILD. Moreover, the phase 1b/2a clinical study of HARS^{WHEP}-Fc (efzofitimod) showed initial positive data in patients with sarcoidosis with steroid tapering (31–33). These findings support the crucial involvement of macrophages in the underlying

pathogenesis and show promise in targeting these cells for the therapeutic intervention of ILD.

Our mechanistic studies revealed that endogenous HARS^{WHEP} is induced by the proinflammatory cytokines TNF- α and IFN- γ . In sarcoidosis, these cytokines are major contributors to chronic inflammation and a series of immunologic cascades involving T cell activation, granuloma formation, expansion, and persistence (47). Our data also showed that HARS^{WHEP}-Fc promotes differentiation of PMDMs with a decreased inflammatory profile without up-regulating typical M1-like or M2-like macrophage markers, which demonstrates its immunomodulatory properties and highlights the plasticity of macrophages (48). HARS^{WHEP}-Fc (efzofitimod) reduces key macrophage-secreted cytokines, such as TNF- α , IL-6, and MCP-1, in the preclinical and clinical studies presented here. These cytokines are critically involved in innate immunity and ILD pathology. For example, in connective tissue disease-associated ILDs including SSc, RA, dermatomyositis, and microscopic polyangiitis-ILD, macrophages modulate the diseases through mechanisms that up-regulate TNF- α , IL-6, and/or MCP-1 (49). MCP-1, the major monocyte-recruiting chemokine, is elevated in the sera and bronchoalveolar lavage fluid (BALF) of patients with ILDs, and its BALF amount has been correlated with disease severity (50, 51). Consistent with the down-regulation of these cytokines/chemokines by HARS^{WHEP}-Fc, in a previous animal study of the LPS acute lung inflammation model, HARS^{WHEP}-Fc reduced infiltrates of immune cells, including alveolar macrophages and inflammatory monocytes, in the bronchoalveolar lavage and lung tissue samples from mice treated with HARS^{WHEP}-Fc (31).

HARS added the WHEP domain at the time of metazoans and retained it thereafter. Of the nine SVs annotated for human HARS, all retain the WHEP domain and, at the same time, ablate the catalytic unit (25). The creation of these catalytic nulls strongly supports the idea of alternative functions for these variants, all of which presumably use the WHEP domain in some way. Here, we focused on the smallest HARS SV, HARS^{WHEP}, which is just 60 amino acids. We found earlier that HARS^{WHEP} was up-regulated in muscle biopsies from patients with dermatomyositis (30). Using an antibody directed against HARS^{WHEP}, we detected the expected 6.8-kDa protein in cultured human cells and estimated its concentration to be about 1% of that of native HARS. Further work showed that the HARS^{WHEP} transcript was present in the 13 different human tissue types, enriched in the lung (30). Consistent with the present work, the release of HARS^{WHEP} to the extracellular space was observed in the circulation of healthy donors (14). These results, the wide tissue distribution, and the present work support the possibility that HARS^{WHEP} has broad utility in modulating the immune system in a variety of tissues.

Our work supports the conclusion that the turn of the HTH motif of the WHEP domain is critical for engagement of NRP2. The WHEP domain has a homolog in four other aaRSs and was originally designated as the WHEP domain using the one-letter abbreviations of the amino acids of the associated synthetases. Later, a fifth synthetase was identified with the same homologous domain. The turn of other WHEP domains, such as those found in glycyl-tRNA synthetase (GARS), tryptophanyl-tRNA synthetase (WARS), methionyl-tRNA synthetase, and glutamyl-prolyl-tRNA synthetase (EPRS), have unique turn sequences that possibly enable engagement with disparate extracellular receptors. This assertion is consistent with the observation that despite high structural conservation between these domains, none of the other aaRS WHEP domains exhibits binding to NRP2, and this interaction is unique to HARS^{WHEP} on the

basis of the SPR binding data presented here. Furthermore, HARS^{WHEP} is entirely selective for NRP2 over the large number of receptors tested, creating the potential that these aaRS domains have evolved to specifically modulate one receptor. The conserved lysine found in all of these turns may be a common anchoring point to members of a group of related or unrelated extracellular receptors that engage the flanking divergent loop residues.

Signaling functions associated with the three WHEP domains of the naturally occurring EPRS fusion protein have been reported. The fusion links together EARS with PARS through tandem WHEP domains. These domains are RNA and protein binding elements that regulate translation of a repertoire of inflammatory genes (52). Human WARS is secreted from monocytes where it interacts with TLR4/macrophage-derived myeloid differentiation protein 2 through the WHEP domain to stimulate chemokine secretion (53, 54). In GARS, its WHEP domain was implicated to suppress an unknown physiological function of GARS, and the Charcot-Marie-Tooth disease-causing genetic variants in *GARS1* (which encodes GARS) might disrupt WHEP-mediated suppression, resulting in gain-of-function disease phenotypes (15, 55).

Our study has several limitations. We performed *in vitro* studies primarily with human peripheral blood cells, which are readily accessible and relevant to the disease (56, 57). Subsequent studies on primary cells in disease-relevant tissue (for example, human bronchoalveolar cells from healthy donors and patients with specific ILD diagnoses) and in collaboration with clinicians or biobanks with access to patient samples could expand the understanding of the immunoregulatory activity and mechanism of action for HARS^{WHEP} in the context of individual disease states. Animal models of pulmonary fibrosis are valuable tools for research, but it is important to recognize that they do not perfectly reflect the heterogeneity and complexities of human disease (58). The bleomycin-induced model of lung fibrosis, for instance, often demonstrates a resolution of fibrosis over time, which is unlike the progressive and irreversible nature of human idiopathic pulmonary fibrosis and, thus, requires dosing regimens that can elucidate efficacy that would not reflect human dosing (59).

Overall, our data demonstrated that HARS^{WHEP} is a homeostatic immunomodulator that reduces inflammation through targeting NRP2 on macrophages, which can subsequently disrupt the cycle of chronic inflammation and fibrosis. This mechanism strengthens the rationale to target ILDs in their inflammatory stages using efzofitimid. Together with clinical proof-of-concept data generated in the phase 1b/2a clinical trial in patients with pulmonary sarcoidosis, our findings highlighted the potential of HARS^{WHEP}-Fc (efzofitimid) as a therapeutic intervention for ILD and related inflammatory disorders through a mechanism of action on macrophages. This preclinical work in combination with clinical data considerably expands the basis for the application of an aaRS SV for treatment of chronic inflammatory conditions, as well as encouraging exploration of other aaRS-based therapies for disease intervention.

MATERIALS AND METHODS

Study design

This study aimed to develop a therapeutic candidate derived from naturally occurring SVs of the aaRS family on the basis of their non-catalytic functions. We focused on one specific SV (HARS^{WHEP}) that was implicated with immunoregulatory functions and associated

with immune-mediated diseases. HARS^{WHEP} was fused to a human IgG Fc for improved pharmacokinetics and evaluated for efficacies on immune cells and in preclinical models of ILDs. We also identified NRP2 as the target receptor of HARS^{WHEP} and determined its up-regulation in differentiated or activated myeloid cells. The mechanism of action for HARS^{WHEP} was further investigated using PMDMs, as well as samples collected from a clinical trial of HARS^{WHEP}-Fc (efzofitimid), in patients with sarcoidosis.

Animal studies performed at aTyr Pharma were governed and approved by aTyr Pharma's Institutional Animal Care and Use Committee (IACUC; protocol: ACUP-100). All treatment and control groups had 10 mice per group, and health checks were performed daily. Body weights were taken once a week, and mice with greater than 20% body weight loss from baseline were carefully assessed for potential euthanasia. Animal studies performed externally were governed and approved by the IACUC of the respective institutions and companies including Biomodels, Charles River, Artimmune, Comparative Biosciences, and FibroCure. Both bleomycin lung injury studies were run in male animals because it has been previously shown that male mice have a greater response to bleomycin injury than female mice regardless of age (60). Except the silicosis model, all other models of experimental ILD were run in female mice for practical purposes such as easier husbandry.

The phase 1b/2a clinical trial (www.clinicaltrials.gov; registry no. NCT03824392) was a randomized, double-blind, placebo-controlled study evaluating multiple ascending doses of efzofitimid in patients with sarcoidosis who underwent a steroid taper. The clinical data and demographics of the cohort were published previously (32). Briefly, patients were dosed with placebo or efzofitimid (1, 3, or 5 mg/kg; $n = 8$ to 12 per group). Clinically meaningful improvements were achieved by efzofitimid in a dose-dependent manner across patient-reported outcomes, several of which reached statistical significance in the dose arm (5 mg/kg) (32). Therefore, the current study focused on comparing the efzofitimid group (5 mg/kg) and the placebo group for serum biomarkers and PBMC transcriptomes. Serum and whole-blood samples were collected at the start (day 1, predose) and end (week 24, posttreatment) of the study (fig. S8A). Patients who missed a scheduled drug dose or missed the week 24 blood draw were excluded from the serum biomarker assay. Five patients in each of the placebo and efzofitimid groups had samples collected on both day 1 and week 24 and qualified (with sufficient PBMC count, viability, and RNA integrity) for the RNA-seq study.

Protein production

HARS^{WHEP}-Fc is the HARS WHEP domain (amino acids 2 to 60) fused with the human IgG1 Fc at the N terminus of HARS^{WHEP}. NH-Fc, which contains amino acids 2 to 11 of HARS and the same Fc fusion as HARS^{WHEP}-Fc, was used as a negative control protein for HARS^{WHEP}-Fc in this study. The drug substance of HARS^{WHEP}-Fc for preclinical studies was produced in the process development laboratories of KBI Biopharma and certified by subsequent analytical testing at KBI. For the clinical study, the GMP-manufactured version of HARS^{WHEP}-Fc (efzofitimid) was used. Recombinant proteins of human NRP2 and monoclonal antibodies against human NRP2 (a-NRP2) were produced as previously described (61).

Screening of cell surface binding target

The cell surface binding target of HARS^{WHEP}-Fc was discovered by a screen of >4500 human plasma membrane proteins at Retrogenix.

Briefly, initial background screens were undertaken to determine the amounts of background binding of HARS^{WHEP}-Fc to HEK293 cells for assessing the suitability, dose, and method for onward screening. Next, in the primary screen, HARS^{WHEP}-Fc was screened for binding against 4550 FL human plasma membrane proteins, each overexpressed in HEK293 cells to identify primary hits. Third, in the confirmation/specificity screen, the vectors encoding the hits were sequenced to confirm their identities. In addition, all primary hits were reexpressed and probed with HARS^{WHEP}-Fc, or other positive and negative controls, to determine repeatability and specificity. Two incubation methods were used in all background, primary, and confirmation screens. The test protein was preincubated with a well-validated Alexa Fluor 647-labeled anti-human IgG Fc detection antibody (2:1 molar ratio) before addition to slides (“preincubation method”), or the same detection antibody was added after the test protein had been incubated and slides were washed (“sequential method”). Binding was assessed by imaging for fluorescence. Hits were classified as very weak, weak, medium, or strong depending on the intensity of the duplicate spots (table S3). Last, a flow cytometry study was performed using live HEK293 transfectants to validate the identified specific interaction partner(s) of HARS^{WHEP}-Fc.

Culture and treatment of PMDMs

PBMCs were purchased from commercial sources or collected from the phase 1b/2a clinical trial (table S8). CD14⁺ CD16⁻ monocytes were isolated from PBMCs by negative selection using the EasySep Human Monocyte Isolation Kit (STEMCELL Technologies). Monocytes were cultured in nontissue culture-treated plates for 3 days with recombinant human M-CSF (10 ng/ml; PeproTech) in RPMI 1640 American Type Culture Collection formulation (Gibco) containing 10% fetal bovine serum (Gibco) for 3 days at 37°C and 5% CO₂. On day 3, an equal volume of fresh medium containing M-CSF (20 ng/ml) was added. PMDMs were cultured for an additional 3 days (M0) and stimulated for 48 hours on day 6 with LPS (100 ng/ml) and IFN- γ (20 ng/ml; M1-like) or IL-4 and IL-13 (20 ng/ml; PeproTech) (M2-like). Cell surface staining and flow cytometry experiments for these cells were performed similarly as for THP-1 cells described in Supplementary Materials and Methods. In antibody blocking experiments, a-HARS^{WHEP} and Fab of the a-NRP2 that targets the b1 domain were used and compared with their respective controls. The a-NRP2 Fab was used instead of the full antibody because of an increased background signal by the full antibody on PMDMs, and the Fab [in the form of F(ab')₂] of a-NRP2 or isotype control was produced by pepsin (Thermo Fisher Scientific) digestion.

Animal models of ILD

Bleomycin model

Mouse bleomycin models were performed by Biomodels. Briefly, male C57BL/6 mice were randomized and assigned to treatment groups of 10 animals each. Bleomycin (2.25 U/kg) in 40 μ l was slowly infused into the lungs through the oropharyngeal route on day 0. Mice were euthanized on day 21, and the lungs were removed for analysis. The left lung lobe was insufflated and fixed in 10% formalin for histological analysis. Fixed lungs were then embedded in paraffin and sectioned at 5 μ m, and slides were stained with MTC for histological examination by an independent veterinary pathologist.

Rat bleomycin models were performed by Charles River. Briefly, Sprague-Dawley rats were dosed with 100 μ l of bleomycin (1 mg/kg) through the oropharyngeal route on days 1 through 7. Mice were

dosed with HARS^{WHEP}-Fc on days 2, 9, and 16. All eight animals per treatment group were euthanized on day 22 for terminal analysis. The right lung lobe was insufflated, excised, and fixed in 10% formalin. Fixed lungs were then embedded in paraffin, sectioned, and stained with hematoxylin and eosin (H&E) for histological examination by an independent veterinary pathologist.

Silica model

The silica (silicosis) model was performed by Artimmune. Briefly, C57BL/6 mice were randomly assigned to treatment groups with 10 study animals each. The mice received a single dose of silica at 2.5 mg per mouse in a volume of 50 μ l through the intratracheal route under isoflurane anesthesia. The mice were either treated weekly with vehicle or HARS^{WHEP}-Fc (3 mg/kg) through the intravenous route until study termination on day 28 after silica administration. The left lung lobe was perfused, excised, and fixed in 4% buffered formalin for 24 hours. After paraffin embedding and sectioning, tissues were stained with MTC for histological analysis. The right lobes were snap-frozen and subsequently homogenized in 1 ml of phosphate-buffered saline (PBS) using an Ultra Turrax homogenizer (IKA: Innovative Laboratory & Process Solutions). Homogenate was centrifuged, and the supernatant was used for soluble collagen content quantitation using the Sircol assay (Biocolor) following the manufacturer's instructions.

CHP model

The *S. rectivirgula* (CHP) model was performed by Comparative Biosciences. Briefly, C57BL/6 female mice were assigned to treatment groups of 10 animals each. The mice were then challenged intranasally with 25 μ g of *S. rectivirgula* antigen (1 mg/ml) 3 consecutive days for 3 weeks. The animals were dosed with vehicle or HARS^{WHEP}-Fc (3 mg/kg) for 3 weeks starting on day -1. The study was terminated on day 20. The right lung lobes were collected, snap-frozen, and subsequently analyzed using a multiplex enzyme-linked immunosorbent assay (ELISA) platform (Luminex). The left lung lobe was perfused, excised, processed for histopathological analysis, and stained with H&E. Tissue sections were examined and scored by a board-certified veterinary pathologist.

Sarcoidosis model

The *P. acnes* (sarcoidosis) model was performed by Comparative Biosciences. Briefly, C57BL/6 female mice were randomized and assigned to treatment groups of 10 animals each and inoculated with 0.25 ml of heat-killed *P. acnes* (2 mg/ml) through the intraperitoneal route. Mice were further inoculated intratracheally with 0.05 ml of heat-killed *P. acnes* on day 14 and day 28. Study animals were dosed with vehicle or HARS^{WHEP}-Fc (3 mg/kg) for 6 weeks covering the entire in-life phase. The study was terminated on day 42. The right lung lobes were collected, snap-frozen, and subsequently analyzed using a multiplex ELISA platform (Luminex). The left lung lobe was perfused, excised, processed for histopathological analysis, and stained with H&E. Tissue sections were examined and scored by a board-certified veterinary pathologist.

The SKG (RA-ILD) model was performed at aTyr. On day 0, SKG/jcl mice were randomized into treatment groups with 10 animals each and received 5 mg of Zymosan through the intraperitoneal route to induce arthritis and associated ILD. Starting on day -1, mice either received vehicle or HARS^{WHEP}-Fc (3 mg/kg) weekly through the intravenous route until the study termination on day 56. At termination, the right lung lobes were collected for immunophenotyping, and the left lung lobe was collected for histopathological and protein analysis.

SSc model

The cGvHd (SSc) model was performed by FibroCure. The B10.D2 → Balb/c [H-2(d)] minor histocompatibility antigen-mismatched model was used, which reflects clinical and pathological symptoms of human sclerodermatous cGvHD. Recipient mice [BALB/c (H-2d)] at 8 weeks of age received total body irradiation with 700 cGy. Six hours after irradiation, all BALB/c (H-2d) recipients received bone marrow from B10.D2 (H-2d) donor mice. For transplantation, 5×10^6 splenocytes and 2×10^6 bone marrow cells from donor mice were resuspended in 0.2 ml of PBS and injected into the tail veins. Seven days after transplantation, the mice were randomized into treatment groups with eight animals each and received weekly intravenous injections of vehicle or HARS^{WHEP}-Fc (0.4 mg/kg) until the EOS on day 56. At necropsy, the right lung lobes were collected for polymerase chain reaction and protein analysis. The left lung lobe was perfused, excised, trimmed, and processed for histopathological analysis. Tissue sections were examined and scored by a board-certified veterinary pathologist.

In the rat lung bleomycin, *P. acnes*, and SKG models, some data points were excluded because the lung was not inflated properly or the stained section was of poor quality. In all animal studies, data points identified as outliers with the Grubbs' test were excluded in the plots (marked in the data file).

RNAscope/IF multiplex

FFPE (formalin-fixed paraffin-embedded) tissue biopsies from pulmonary sarcoidosis and patients with SSc (table S9) were evaluated for RNA expression of *NRP2* transcript variant 6 and *ITGAM* transcript variant 1 (CD11b) and protein expression of CD68 and CD163 by RNAscope LS multiplex sequential in situ hybridization (ISH)/IF assay for mRNA and protein codetection by Advanced Cell Diagnostics Inc., performed on the Leica BOND RX automation platform using the RNAscope LS multiplex fluorescent reagent kit. Briefly, 5- μ m FFPE tissue sections were pretreated with heat, target/antigen retrieval, and protease before hybridization with the target oligo probes. First, preamplifier and amplifier were hybridized sequentially, followed by trichostatin A (TSA)-fluorophore reaction. Each mRNA channel reacts with a unique fluorophore. After the ISH protocol, IF was performed sequentially with primary antibody incubation followed by secondary antibody, polymer, and then TSA-fluorophore to visualize the signal. The first primary was then stripped, followed by incubation of the second primary antibody, secondary antibody, polymer, and then TSA-fluorophore. Samples were counterstained with 4',6-diamidino-2-phenylindole (DAPI). Each sample was quality controlled for RNA integrity with an RNAscope positive control probe specific to human and for background with a probe specific to bacterial *dapB* RNA. Images were acquired at 40 \times using appropriate fluorescent filters on the PANNORAMIC SCAN II (3D Histech). Specific RNA staining signal was identified as fluorescent, punctate dots. Specific protein staining was defined by distinct membrane or cytoplasmic staining.

Semiquantitative scoring of NRP2 in patient tissue macrophages

H-scoring for NRP2 was performed on pulmonary sarcoidosis lung and SSc skin samples by a board-certified pathologist. H-scoring was performed visually to assess the predominant staining pattern across the entire sample. Cells were grouped into five bins on the basis of the number of dots per cell, and the percentage of cells in each bin was scored. The H-score was calculated by totaling the percentage

of cells in each bin according to the weighted formula below. H-scores are provided on a scale of 0 to 400. $H\text{-Score} = 0 \times (\% \text{ of cells in bin } 0) + 1 \times (\% \text{ of cells in bin } 1) + 2 \times (\% \text{ of cells in bin } 2) + 3 \times (\% \text{ of cells in bin } 3) + 4 \times (\% \text{ of cells in bin } 4)$.

Serum biomarker analysis

Serum samples were collected from patients with pulmonary sarcoidosis before receiving the first dose (day 1) of efzofitimod (5 mg/kg) or placebo and after 24 weeks (EOS) of treatment. Each serum sample was stored frozen until analysis and was tested in duplicate using the MSD V-Plex Human Biomarker 40-Plex Kit (catalog no. 15209D) according to kit instructions. Results were analyzed on GraphPad Prism, and sample values were calculated using an interpolated standard curve. If results were above the range of the assay, the supernatant was further diluted and reevaluated. Fold change was calculated by dividing the EOS value by the day one value.

Statistical analysis

The statistical analysis for comparing two groups was performed using unpaired *t* tests (GraphPad Prism). Patient serum biomarker amounts before and after treatment were analyzed by paired *t* test using Prism. Multiple groups were analyzed by one-way or two-way analysis of variance (ANOVA) followed with multiple comparisons tests using Prism. Means were taken to be significantly different if $P < 0.05$. In figures, * indicates $P < 0.05$, ** indicates $P < 0.01$, *** indicates $P < 0.001$, and **** indicates $P < 0.0001$ for the indicated pairwise comparison. In the transcriptome pathway analysis, significance was determined by GSEA and defined as normalized $P < 0.05$ and normalized FDR *q* value < 0.2 .

Supplementary Materials**The PDF file includes:**

Materials and Methods

Figs. S1 to S9

Tables S1 to S11

References (62–73)

Other Supplementary Material for this manuscript includes the following:

Data files S1 to S3

MDAR Reproducibility checklist

REFERENCES AND NOTES

1. K. M. Antoniou, G. A. Margaritopoulos, S. Tomassetti, F. Bonella, U. Costabel, V. Poletti, Interstitial lung disease. *Eur. Respir. Rev.* **23**, 40–54 (2014).
2. M. Wijsenbeek, A. Suzuki, T. M. Maher, Interstitial lung diseases. *Lancet* **400**, 769–786 (2022).
3. N. Jeganathan, M. Sathanathan, The prevalence and burden of interstitial lung diseases in the USA. *ERJ Open Res.* **8**, 00630–02021 (2022).
4. M. Wijsenbeek, V. Cottin, Spectrum of fibrotic lung diseases. *N. Engl. J. Med.* **383**, 958–968 (2020).
5. A. S. Galindo-Feria, A. Notarnicola, I. E. Lundberg, B. Horuluoglu, Aminoacyl-tRNA synthetases: On anti-synthetase syndrome and beyond. *Front. Immunol.* **13**, 866087 (2022).
6. L. Jiang, J. Jones, X. L. Yang, Human diseases linked to cytoplasmic aminoacyl-tRNA synthetases. *Enzyme* **48**, 277–319 (2020).
7. P. Yao, P. L. Fox, Aminoacyl-tRNA synthetases in medicine and disease. *EMBO Mol. Med.* **5**, 332–343 (2013).
8. S. G. Park, P. Schimmel, S. Kim, Aminoacyl tRNA synthetases and their connections to disease. *Proc. Natl. Acad. Sci. U.S.A.* **105**, 11043–11049 (2008).
9. M. Guo, P. Schimmel, Essential nontranslational functions of tRNA synthetases. *Nat. Chem. Biol.* **9**, 145–153 (2013).
10. J. Chen, Arginyl-tRNA synthetase in inflammation. *Nat. Cell Biol.* **25**, 520–521 (2023).

11. E. Y. Lee, S. M. Kim, J. H. Hwang, S. Y. Jang, S. Park, S. Choi, G. S. Lee, J. Hwang, J. H. Moon, P. L. Fox, S. Kim, C. H. Lee, M. H. Kim, Glutamyl-prolyl-tRNA synthetase 1 coordinates early endosomal anti-inflammatory AKT signaling. *Nat. Commun.* **13**, 6455 (2022).
12. Y. Morodomi, S. Kanaji, B. M. Sullivan, A. Zarpellon, J. N. Orje, E. Won, R. Shapiro, X. L. Yang, W. Ruf, P. Schimmel, Z. M. Ruggeri, T. Kanaji, Inflammatory platelet production stimulated by tyrosyl-tRNA synthetase mimicking viral infection. *Proc. Natl. Acad. Sci. U.S.A.* **119**, e2212659119 (2022).
13. Y. Sung, I. Yoon, J. M. Han, S. Kim, Functional and pathologic association of aminoacyl-tRNA synthetases with cancer. *Exp. Mol. Med.* **54**, 553–566 (2022).
14. R. A. Adams, C. Fernandes-Cerqueira, A. Notarnicola, E. Mertsching, Z. Xu, W. S. Lo, K. Ogilvie, K. P. Chiang, J. Ampudia, S. Rosengren, A. Cubitt, D. J. King, J. D. Mendlein, X. L. Yang, L. A. Nangle, I. E. Lundberg, P. J. Jakobsson, P. Schimmel, Serum-circulating His-tRNA synthetase inhibits organ-targeted immune responses. *Cell. Mol. Immunol.* **18**, 1463–1475 (2021).
15. N. Wei, Q. Zhang, X. L. Yang, Neurodegenerative Charcot-Marie-Tooth disease as a case study to decipher novel functions of aminoacyl-tRNA synthetases. *J. Biol. Chem.* **294**, 5321–5339 (2019).
16. V. Boczonadi, M. J. Jennings, R. Horvath, The role of tRNA synthetases in neurological and neuromuscular disorders. *FEBS Lett.* **592**, 703–717 (2018).
17. K. Wakasugi, P. Schimmel, Two distinct cytokines released from a human aminoacyl-tRNA synthetase. *Science* **284**, 147–151 (1999).
18. M. Guo, X. L. Yang, Architecture and metamorphosis. *Top. Curr. Chem.* **344**, 89–118 (2014).
19. M. Guo, X. L. Yang, P. Schimmel, New functions of aminoacyl-tRNA synthetases beyond translation. *Nat. Rev. Mol. Cell Biol.* **11**, 668–674 (2010).
20. X. Xu, Y. Shi, H. M. Zhang, E. C. Swindell, A. G. Marshall, M. Guo, S. Kishi, X. L. Yang, Unique domain appended to vertebrate tRNA synthetase is essential for vascular development. *Nat. Commun.* **3**, 681 (2012).
21. R. W. Burgess, E. Storkebaum, tRNA dysregulation in neurodevelopmental and neurodegenerative diseases. *Annu. Rev. Cell Dev. Biol.* **39**, 223–252 (2023).
22. A. K. Turvey, G. A. Horvath, A. R. O. Cavalcanti, Aminoacyl-tRNA synthetases in human health and disease. *Front. Physiol.* **13**, 1029218 (2022).
23. P. Schimmel, The endless frontier of tRNA synthetases. *Enzyme* **48**, 1–10 (2020).
24. Z. Xu, W. S. Lo, D. B. Beck, L. A. Schuch, M. Olahova, R. Kopajtic, Y. E. Chong, C. L. Alston, E. Seidl, L. Zhai, C. F. Lau, D. Timchak, C. A. LeDuc, A. C. Borczuk, A. F. Teich, J. Juusola, C. Sofoso, C. Muller, G. Pierre, T. Hilliard, P. D. Turnpenny, M. Wagner, M. Kappler, F. Brasch, J. P. Bouffard, L. A. Nangle, X. L. Yang, M. Zhang, R. W. Taylor, H. Prokisch, M. Griese, W. K. Chung, P. Schimmel, Bi-allelic mutations in Phe-tRNA synthetase associated with a multi-system pulmonary disease support non-translational function. *Am. J. Hum. Genet.* **103**, 100–114 (2018).
25. W. S. Lo, E. Gardiner, Z. Xu, C. F. Lau, F. Wang, J. J. Zhou, J. D. Mendlein, L. A. Nangle, K. P. Chiang, X. L. Yang, K. F. Au, W. H. Wong, M. Guo, M. Zhang, P. Schimmel, Human tRNA synthetase catalytic nulls with diverse functions. *Science* **345**, 328–332 (2014).
26. A. Hegde, V. Marwah, S. V. R. Choudhary, V. Malik, Anti-Jo1 syndrome: Understanding a rare cause of interstitial lung disease. *Mediterr. J. Rheumatol.* **33**, 437–443 (2022).
27. A. L. Mammen, Autoimmune myopathies: Autoantibodies, phenotypes and pathogenesis. *Nat. Rev. Neurol.* **7**, 343–354 (2011).
28. L. Cavagna, L. Nuno, C. A. Scire, M. Govoni, F. J. L. Longo, F. Franceschini, R. Neri, S. Castaneda, W. A. S. Giraldo, R. Caporali, F. Iannone, E. Fusaro, G. Paolazzi, R. Pellerito, A. Schwarting, L. A. Saketkoo, N. Ortego-Centeno, L. Quartuccio, E. Bartoloni, C. Specker, T. P. Murcia, R. La Corte, F. Furini, V. Foschi, J. B. Corral, P. Airo, I. Cavazzana, J. Martinez-Barrio, M. Hinojosa, M. Giannini, S. Barsotti, J. Menke, K. Triantafyllias, R. Vitetta, A. Russo, G. Bajocchi, E. Bravi, G. Barausse, R. Bortolotti, C. Selmi, S. Parisi, C. Montecucco, M. A. Gonzalez-Gay, AENEAS (American, European Network of Antisynthetase Syndrome) collaborative group, Clinical spectrum time course in anti Jo-1 positive antisynthetase syndrome: Results from an international retrospective multicenter study. *Medicine* **94**, e1144 (2015).
29. S. M. Levine, N. Raben, D. Xie, F. B. Askin, R. Tuder, M. Mullins, A. Rosen, L. A. Casciola-Rosen, Novel conformation of histidyl-transfer RNA synthetase in the lung: The target tissue in Jo-1 autoantibody-associated myositis. *Arthritis Rheum.* **56**, 2729–2739 (2007).
30. J. J. Zhou, F. Wang, Z. Xu, W. S. Lo, C. F. Lau, K. P. Chiang, L. A. Nangle, M. A. Ashlock, J. D. Mendlein, X. L. Yang, M. Zhang, P. Schimmel, Secreted histidyl-tRNA synthetase splice variants elaborate major epitopes for autoantibodies in inflammatory myositis. *J. Biol. Chem.* **289**, 19269–19275 (2014).
31. R. P. Baughman, V. Niranjan, G. Walker, C. Burkart, S. Paz, Y. Chong, D. Siefker, E. Sun, L. Nangle, S. Forster, M. Muters, C. Farver, E. Lower, S. Shukla, D. A. Culver, Efozotimid: A novel anti-inflammatory agent for sarcoidosis. *Sarcoidosis Vasc. Diffuse Lung Dis.* **40**, e2023011 (2023).
32. D. A. Culver, S. Aryal, J. Barney, C. C. W. Hsia, W. E. James, L. A. Maier, L. T. Marts, O. N. Obi, P. H. S. Sporn, N. J. Sweiss, S. Shukla, N. Kinnersley, G. Walker, R. Baughman, Efozotimid for the treatment of pulmonary sarcoidosis. *Chest* **163**, 881–890 (2023).
33. G. Walker, R. Adams, L. Guy, A. Chandrasekaran, N. Kinnersley, P. Ramesh, L. Zhang, F. Brown, V. Niranjan, Exposure-response analyses of efozotimid in patients with pulmonary sarcoidosis. *Front. Pharmacol.* **14**, 1258236 (2023).
34. J. Katzen, M. F. Beers, Contributions of alveolar epithelial cell quality control to pulmonary fibrosis. *J. Clin. Invest.* **130**, 5088–5099 (2020).
35. T. Parimon, C. Yao, B. R. Stripp, P. W. Noble, P. Chen, Alveolar epithelial type II cells as drivers of lung fibrosis in idiopathic pulmonary fibrosis. *Int. J. Mol. Sci.* **21**, 2269 (2020).
36. R. C. Stone, I. Pastar, N. Ojeh, V. Chen, S. Liu, K. I. Garzon, M. Tomic-Canic, Epithelial-mesenchymal transition in tissue repair and fibrosis. *Cell Tissue Res.* **365**, 495–506 (2016).
37. H. Ihara, Y. Mitsuishi, M. Kato, F. Takahashi, K. Tajima, T. Hayashi, M. Hidayat, W. Winardi, A. Wirawan, D. Hayakawa, K. Kanamori, N. Matsumoto, T. Yae, T. Sato, S. Sasaki, K. Takamochi, Y. Suehara, D. Ogura, S. I. Niwa, K. Suzuki, K. Takahashi, Nintedanib inhibits epithelial-mesenchymal transition in A549 alveolar epithelial cells through regulation of the TGF-beta/Smad pathway. *Respir. Investig.* **58**, 275–284 (2020).
38. Z. Xu, Z. Wei, J. J. Zhou, F. Ye, W. S. Lo, F. Wang, C. F. Lau, J. A. Nangle, K. P. Chiang, X. L. Yang, M. Zhang, P. Schimmel, Internally deleted human tRNA synthetase suggests evolutionary pressure for repurposing. *Structure* **20**, 1470–1477 (2012).
39. H. F. Guo, C. W. Vander Kooi, Neuropilin functions as an essential cell surface receptor. *J. Biol. Chem.* **290**, 29120–29126 (2015).
40. S. Roy, A. K. Bag, R. K. Singh, J. E. Talmadge, S. K. Batra, K. Datta, Multifaceted role of neuropilins in the immune system: Potential targets for immunotherapy. *Front. Immunol.* **8**, 1228 (2017).
41. R. P. Baughman, S. Field, U. Costabel, R. G. Crystal, D. A. Culver, M. Drent, M. A. Judson, G. Wolff, Sarcoidosis in America. Analysis based on health care use. *Ann. Am. Thorac. Soc.* **13**, 1244–1252 (2016).
42. S. Forster, Y. E. Chong, D. Siefker, Y. Becker, R. Bao, E. Escobedo, Y. Qing, K. Rauch, L. Burman, C. Burkart, P. Kainz, A. Cubitt, M. Muters, L. A. Nangle, Development and characterization of a novel neuropilin-2 antibody for immunohistochemical staining of cancer and sarcoidosis tissue samples. *Monoclon. Antib. Immunodiagn. Immunother.* **42**, 157–165 (2023).
43. A. M. Newman, C. B. Steen, C. L. Liu, A. J. Gentles, A. A. Chaudhuri, F. Scherer, M. S. Khodadoust, M. S. Esfahani, B. A. Luca, D. Steiner, M. Diehn, A. A. Alizadeh, Determining cell type abundance and expression from bulk tissues with digital cytometry. *Nat. Biotechnol.* **37**, 773–782 (2019).
44. A. Bergamasco, N. Hartmann, L. Wallace, P. Verpillat, Epidemiology of systemic sclerosis and systemic sclerosis-associated interstitial lung disease. *Clin. Epidemiol.* **11**, 257–273 (2019).
45. V. Liakouli, A. Ciancio, F. Del Galdo, R. Giacomelli, F. Ciccia, Systemic sclerosis interstitial lung disease: Unmet needs and potential solutions. *Nat. Rev. Rheumatol.* **20**, 21–32 (2024).
46. A. J. Byrne, T. M. Maher, C. M. Lloyd, Pulmonary macrophages: A new therapeutic pathway in fibrosing lung disease? *Trends Mol. Med.* **22**, 303–316 (2016).
47. O. N. Obi, L. A. Saketkoo, A. M. Russell, R. P. Baughman, Sarcoidosis: Updates on therapeutic drug trials and novel treatment approaches. *Front. Med.* **9**, 991783 (2022).
48. Z. Strizova, I. Benesova, R. Bartolini, R. Novysek, E. Cecrdlova, L. K. Foley, I. Striz, M1/M2 macrophages and their overlaps - myth or reality? *Clin. Sci.* **137**, 1067–1093 (2023).
49. C. C. Tseng, Y. W. Sung, K. Y. Chen, P. Y. Wang, C. Y. Yen, W. Y. Sung, C. C. Wu, T. T. Ou, W. C. Tsai, W. T. Liao, C. J. Chen, S. C. Lee, S. J. Chang, J. H. Yen, The role of macrophages in connective tissue disease-associated interstitial lung disease: Focusing on molecular mechanisms and potential treatment strategies. *Int. J. Mol. Sci.* **24**, 11995 (2023).
50. D. Hartl, M. Griese, T. Nicolai, G. Zissel, C. Prell, D. Reinhardt, D. J. Schendel, S. Krauss-Etschmann, A role for MCP-1/CCR2 in interstitial lung disease in children. *Respir. Res.* **6**, 93 (2005).
51. M. Suga, K. Iyonaga, H. Ichiyasu, N. Saita, H. Yamasaki, M. Ando, Clinical significance of MCP-1 levels in BALF and serum in patients with interstitial lung diseases. *Eur. Respir. J.* **14**, 376–382 (1999).
52. J. Jia, A. Arif, P. S. Ray, P. L. Fox, WHEP domains direct noncanonical expression of glutamyl-Prolyl tRNA synthetase in translational control of gene expression. *Mol. Cell* **29**, 679–690 (2008).
53. Y. H. Ahn, S. Park, J. J. Choi, B. K. Park, K. H. Rhee, E. Kang, S. Ahn, C. H. Lee, J. S. Lee, K. S. Inn, M. L. Cho, S. H. Park, K. Park, H. J. Park, J. H. Lee, J. W. Park, N. H. Kwon, H. Shim, B. W. Han, P. Kim, J. Y. Lee, Y. Jeon, J. W. Huh, M. Jin, S. Kim, Secreted tryptophanyl-tRNA synthetase as a primary defence system against infection. *Nat. Microbiol.* **2**, 16191 (2016).
54. M. Jin, Unique roles of tryptophanyl-tRNA synthetase in immune control and its therapeutic implications. *Exp. Mol. Med.* **51**, 1–10 (2019).
55. S. J. Grice, J. N. Sleight, W. W. Motley, J. L. Liu, R. W. Burgess, K. Talbot, M. Z. Cader, Dominant, toxic gain-of-function mutations in gars lead to non-cell autonomous neuropathology. *Hum. Mol. Genet.* **24**, 4397–4406 (2015).
56. K. Yoshioka, H. Sato, T. Kawasaki, D. Ishii, T. Imamoto, M. Abe, Y. Hasegawa, O. Ohara, K. Tatsumi, T. Suzuki, Transcriptome analysis of peripheral blood mononuclear cells in pulmonary sarcoidosis. *Front. Med.* **9**, 822094 (2022).

57. B. Min, A. Grant-Orser, K. A. Johansson, Peripheral blood monocyte count and outcomes in patients with interstitial lung disease: A systematic review and meta-analysis. *Eur. Respir. Rev.* **32**, 230072 (2023).
58. J. Padmanabhan, Z. N. Maan, S. H. Kwon, R. Kosaraju, C. A. Bonham, G. C. Gurtner, In vivo models for the study of fibrosis. *Adv. Wound Care* **8**, 645–654 (2019).
59. G. Bohn, B. Liden, G. Schultz, Q. Yang, D. J. Gibson, Ovine-based collagen matrix dressing: Next-generation collagen dressing for wound care. *Adv. Wound Care* **5**, 1–10 (2016).
60. E. F. Redente, K. M. Jacobsen, J. J. Solomon, A. R. Lara, S. Faubel, R. C. Keith, P. M. Henson, G. P. Downey, D. W. Riches, Age and sex dimorphisms contribute to the severity of bleomycin-induced lung injury and fibrosis. *Am. J. Physiol. Lung Cell. Mol. Physiol.* **301**, L510–L518 (2011).
61. Z. Xu, H. L. Goel, C. Burkart, L. Burman, Y. E. Chong, A. G. Barber, Y. Geng, L. Zhai, M. Wang, A. Kumar, A. Menefee, C. Polizzi, L. Eide, K. Rauch, J. Rahman, K. Hamel, Z. Fogassy, S. Klopp-Savino, S. Paz, M. Zhang, A. Cubitt, L. A. Nangle, A. M. Mercurio, Inhibition of VEGF binding to neuropilin-2 enhances chemosensitivity and inhibits metastasis in triple-negative breast cancer. *Sci. Transl. Med.* **15**, eadf1128 (2023).
62. J. Vandesompele, K. De Preter, F. Pattyn, B. Poppe, N. Van Roy, A. De Paepe, F. Speleman, Accurate normalization of real-time quantitative RT-PCR data by geometric averaging of multiple internal control genes. *Genome Biol.* **3**, research0034.1 (2002).
63. W. Minor, M. Cymborowski, Z. Otwinowski, M. Chruszcz, HKL-3000: The integration of data reduction and structure solution—from diffraction images to an initial model in minutes. *Acta Crystallogr. D Biol. Crystallogr.* **62**, 859–866 (2006).
64. A. J. McCoy, R. W. Grosse-Kunstleve, P. D. Adams, M. D. Winn, L. C. Storoni, R. J. Read, Phaser crystallographic software. *J. Appl. Cryst.* **40**, 658–674 (2007).
65. M. D. Winn, C. C. Ballard, K. D. Cowtan, E. J. Dodson, P. Emsley, P. R. Evans, R. M. Keegan, E. B. Krissinel, A. G. Leslie, A. McCoy, S. J. McNicholas, G. N. Murshudov, N. S. Pannu, E. A. Potterton, H. R. Powell, R. J. Read, A. Vagin, K. S. Wilson, Overview of the CCP4 suite and current developments. *Acta Crystallogr. D Biol. Crystallogr.* **67**, 235–242 (2011).
66. P. Emsley, K. Cowtan, Coot: Model-building tools for molecular graphics. *Acta Crystallogr. D Biol. Crystallogr.* **60**, 2126–2132 (2004).
67. G. N. Murshudov, A. A. Vagin, E. J. Dodson, Refinement of macromolecular structures by the maximum-likelihood method. *Acta Crystallogr. D Biol. Crystallogr.* **53**, 240–255 (1997).
68. Z. Otwinowski, W. Minor, Processing of X-ray diffraction data collected in oscillation mode. *Methods Enzymol.* **276**, 307–326 (1997).
69. A. Vagin, A. Teplyakov, Molecular replacement with MOLREP. *Acta Crystallogr. D Biol. Crystallogr.* **66**, 22–25 (2010).
70. D. Liebschner, P. V. Afonine, M. L. Baker, G. Bunkoczi, V. B. Chen, T. I. Croll, B. Hintze, L. W. Hung, S. Jain, A. J. McCoy, N. W. Moriarty, R. D. Oeffner, B. K. Poon, M. G. Prisant, R. J. Read, J. S. Richardson, D. C. Richardson, M. D. Sammito, O. V. Sobolev, D. H. Stockwell, T. C. Terwilliger, A. G. Urzhumtsev, L. L. Videau, C. J. Williams, P. D. Adams, Macromolecular structure determination using x-rays, neutrons and electrons: Recent developments in Phenix. *Acta Crystallogr. D Struct. Biol.* **75**, 861–877 (2019).
71. T. Metsalu, J. Vilo, ClustVis: A web tool for visualizing clustering of multivariate data using principal component analysis and heatmap. *Nucleic Acids Res.* **43**, W566–W570 (2015).
72. A. Subramanian, P. Tamayo, V. K. Mootha, S. Mukherjee, B. L. Ebert, M. A. Gillette, A. Paulovich, S. L. Pomeroy, T. R. Golub, E. S. Lander, J. P. Mesirov, Gene set enrichment analysis: A knowledge-based approach for interpreting genome-wide expression profiles. *Proc. Natl. Acad. Sci. U.S.A.* **102**, 15545–15550 (2005).
73. P. Shannon, A. Markiel, O. Ozier, N. S. Baliga, J. T. Wang, D. Ramage, N. Amin, B. Schwikowski, T. Ideker, Cytoscape: A software environment for integrated models of biomolecular interaction networks. *Genome Res.* **13**, 2498–2504 (2003).

Acknowledgments

Funding: Financial support for this study was provided by aTyr Pharma. P.S. acknowledges support by a fellowship from the National Foundation for Cancer Research. **Author contributions:** L.A.N. and P.S. conceptualized the study; L.A.N. and M.Z. administered the project and coordinated resources; L.A.N., Z.X., D.K., M.-H.D., and M.Z. designed, supervised, and audited experiments across aTyr Pharma and IAS HKUST/Pangu Biopharma. Z.X. and S.C. designed SV characterization studies, and Y.T. and S.K.-S. performed the experiments. K.P.C., R.A., S.C., Y.E.C., and Z.X. performed experiments to validate target receptor interactions. D.L. established methodology for protein purification and performed purification. L.Z. and Y.G. performed and analyzed structural studies. K.R. and L.B. performed molecular biology experiments and domain swapping. L.B., Y.E.C., and K.H. designed and performed dimerization experiments. Y.E.C. designed and performed target protein interaction studies. S.P., Z.X., and D.S. designed primary cell experiments and flow cytometry, and D.S., M.F., S.K.-S., and A.W. performed experiments. Z.X. performed RNA expression and pathway analysis. R.A. designed and analyzed circulating cytokine and secreted cytokines, and L.G. performed experiments and analyzed the data. K.O. and C.B. designed and supervised preclinical animal experiments, C.P. and L.E. performed internal experiments, and C.P. analyzed resulting histology data. S.P., Z.X., D.S., and Y.E.C. designed and analyzed patient-derived staining experiments, and D.S. performed internal flow cytometry experiments on these cells. L.A.N., Z.X., D.S., C.B., Y.E.C., and P.S. wrote the manuscript. **Competing interests:** Efozotimod is covered by patent families listed in data file S3: Compositions and methods comprising histidyl-tRNA synthetase splice variants having non-canonical biological activities (patent numbers 2010226726, 2755784, 2408905, 2408905, 2408905, 2408905, 2408905, 2408905, 1166641, 2408905, 5730280, 8404242, 3255146, 201510024397.2, 3255146, 3255146, 3255146, 3255146, 3255146, 3255146, HK1247243 6166241, 8753638, 9605265, 10017582, 10526419, 10941214, and 11078299; L.A.N. and Z.X. are inventors), Histidyl-tRNA synthetase-Fc conjugates (patent numbers 2014233436, 2907046, 2970921, 201480026024.2, 2970921, 2970921, 2970921, 2970921, 2970921, HK1220226, 2970921, 6397479, 9587235, 3460054, 3460054, 3460054, 3460054, 3460054, HK40006273, 3460054, 6687692, 10093915, 10472618, 10711260, and 11072787; K.P.C. and M.-H.D. are inventors), and Compositions and methods for treating lung inflammation (patent number 11767520; K.O. is an inventor). All authors were employed or associated with aTyr Pharma when conducting research for this study. Pursuant to their employment, all current employees of aTyr Pharma have stock options in the company. L.A.N., K.P.C., and P.S. own stock in aTyr Pharma. **Data and materials availability:** All data associated with this study are present in the paper or the supplementary materials. The structural data are available through the PDB (8YP1 and 8YOR). We will provide HARS^{WHEP}-Fc, NH-Fc, and in-house antibodies used in this study for research through a materials transfer agreement.

Submitted 26 March 2024

Resubmitted 24 September 2024

Accepted 19 February 2025

Published 12 March 2025

10.1126/scitranslmed.adp4754